Magnetic fields in the early stages of massive star formation as revealed by ALMA

Junhao Liu,[1,2,3] Qizhou Zhang,[3] Keping Qiu,[1,2] Hauyu Baobab Liu,[4] Thushara Pillai,[5,6] Josep Miquel Girart,[7,8] Zhi-Yun Li,[9] and Ke Wang[10]

[1]*School of Astronomy and Space Science, Nanjing University, 163 Xianlin Avenue, Nanjing, Jiangsu 210023, People's Republic of China*
[2]*Key Laboratory of Modern Astronomy and Astrophysics (Nanjing University), Ministry of Education, Nanjing, Jiangsu 210023, People's Republic of China*
[3]*Center for Astrophysics | Harvard & Smithsonian, 60 Garden Street, Cambridge, MA 02138, USA*
[4]*Academia Sinica Institute of Astronomy and Astrophysics, P.O. Box 23-141, Taipei 10617, Taiwan*
[5]*Max-Planck-Institut für Radioastronomie, Auf dem Hügel 69, 53121 Bonn, Germany*
[6]*Institute for Astrophysical Research, 725 Commonwealth Ave, Boston University Boston, MA 02215, USA*
[7]*Institut de Ciències de l'Espai (ICE, CSIC), Can Magrans s/n, E-08193 Cerdanyola del Vallès, Catalonia*
[8]*Institut d'Estudis Espacials de de Catalunya (IEEC), E-08034 Barcelona, Catalonia*
[9]*Astronomy Department, University of Virginia, Charlottesville, VA 22904-4325, USA*
[10]*Kavli Institute for Astronomy and Astrophysics, Peking University, 5 Yiheyuan Road, Haidian District, Beijing 100871, People's Republic of China*

ABSTRACT

We present 1.3 mm ALMA dust polarization observations at a resolution of $\sim$0.02 pc of three massive molecular clumps, MM1, MM4, and MM9, in the infrared dark cloud G28.34+0.06. With the sensitive and high-resolution continuum data, MM1 is resolved into a cluster of condensations. The magnetic field structure in each clump is revealed by the polarized emission. We found a trend of decreasing polarized emission fraction with increasing Stokes I intensities in MM1 and MM4. Using the angular dispersion function method (a modified Davis-Chandrasekhar-Fermi method), the plane-of-sky magnetic field strength in two massive dense cores, MM1-Core1 and MM4-Core4, are estimated to be $\sim$1.6 mG and $\sim$0.32 mG, respectively. **The ordered magnetic energy is found to be smaller than the turbulent energy in the two cores, while the total magnetic energy is found to be comparable to the turbulent energy.** The total virial parameters in MM1-Core1 and MM4-Core4 are calculated to be $\sim$0.76 and $\sim$0.37, respectively, suggesting that massive star formation does not start in equilibrium. Using the polarization-intensity gradient-local gravity method, we found that the local gravity is closely aligned with intensity gradient in the three clumps, and the magnetic field tends to be aligned with the local gravity in MM1 and MM4 except for regions near the emission peak, which suggests that the gravity plays a dominant role in regulating the gas collapse. Half of the outflows in MM4 and MM9 are found to be aligned within 10° of the condensation-scale ($<$0.05 pc) magnetic field, indicating that the magnetic field could play an important role from condensation to disk scale in the early stage of massive star formation. We also find that the fragmentation in MM1-Core1 cannot be solely explained by thermal Jeans fragmentation or turbulent Jeans fragmentation. **(Some contents edited after publication.)**

Keywords: polarization — magnetic fields — ISM: individual objects (IRDC G28.34+0.06) — stars: formation

1. INTRODUCTION

It is clear that stars are formed from the collapse of molecular dense cores[1] that are created by the con-

---

[1] Following the nomenclature in Zhang et al. (2009), we refer to a molecular clump as an entity of $\sim$ 1 pc, a dense core as an entity of $\sim$ 0.1 pc, and a condensation as an entity of $\sim$ 0.01 pc that forms one star or a group of stars.

Corresponding author: Keping Qiu
kpqiu@nju.edu.cn

traction of over dense regions in molecular clouds when gravity overcomes the internal pressure such as magnetic fields or turbulence (Shu et al. 1987). In the formation of massive stars (mass $> 8\ M_\odot$), turbulence is believed to play an important role because massive star-forming regions are usually found to be supersonic and have large line widths. However, the role of magnetic fields in massive star formation is still not well understood (Krumholz 2014; Tan et al. 2014; Hull, & Zhang 2019; Pattle & Fissel 2019).

The Radiative Alignment Torque (RAT) theory predicts that asymmetrical dust grains with sizes $>0.05\ \mu m$ are expected to spin-up due to the radiative torque in the presence of a radiation field and the short axis of these dust grains would tend to be aligned with magnetic field lines (Lazarian 2007; Lazarian, & Hoang 2007). Theoretical and observational evidence has supported the RAT mechanism as the dominant grain alignment mechanism to produce polarized thermal emission at millimeter/sub-millimeter (mm/submm) wavelengths in diffuse intersteller medium and molecular clouds with μm or sub-μm size grains (Andersson et al. 2015). The exception is that the grain size grows to millimeter/sub-millimeter in protoplanetary disks and the observed polarization would be dominated by those produced from dust self-scattering (Kataoka et al. 2015; Yang et al. 2016) or grains aligned by strong radiation fields (Tazaki et al. 2017). Thus, observing the polarized dust emission at mm/sub-mm offers a powerful way to trace the plane-of-sky magnetic field in star-forming molecular clouds at scales greater than the disk scales.

In the past two decades, there has been an increasing number of high-resolution and high-sensitivity observational studies of the dust polarization in high-mass star-forming regions (for a detailed review see Hull, & Zhang 2019). A variety of field structures from hourglass-like shapes (e.g., G31.41, G240.31, OMC 1, Girart et al. 2009; Qiu et al. 2014; Ward-Thompson et al. 2017) to more complex and chaotic morphologies (e.g., Orion KL, G5.89, Rao et al. 1998; Tang et al. 2009) have been reported by these studies. The magnetic field in massive star-forming regions is found to be dynamically important from the clump scale to the core scale and the core scale magnetic field does not show strong correlation with the outflow axis (Zhang et al. 2014). Quantitatively, the magnetic field plays an important role in supporting the massive dense cores against gravitational collapse (Girart et al. 2013; Frau et al. 2014).

Despite the significant progress made by the recent polarization observations of massive star formation regions, most of these studies of magnetic fields targeted evolved star-forming regions. Due to the relatively weak

polarized dust emission and the limitation of instrumental sensitivity, there are only a handful of single-dish case studies about the magnetic field in early massive star formation regions (Pillai et al. 2015; Juvela et al. 2018; Liu et al. 2018; Tang et al. 2019; Soam et al. 2019) and there is only one inteferometric study of the magnetic field at the onset of massive star formation in the infrared dark cloud 18310-4 where the magnetic field structure is not well resolved (Beuther et al. 2018). The role of magnetic fields in the initial stage of massive star formation remains an open question.

There are two distinct models of massive star formation. The turbulent core accretion model (McKee, & Tan 2002) envisioned that massive stars are formed via the monolithic collapse of massive dense cores in virial equilibrium, where the pressure support comes from turbulence and the magnetic field (Tan et al. 2013). Alternatively, the competitive accretion model (Bonnell et al. 1997) proposed that a cluster of low-mass protostars compete with one another to accrete from the natal gas reservoir and the protostars near the center of gravitational potential accreting at higher rates can thus form massive stars. Krumholz et al. (2005) showed that a sub-virial state is required for the competitive accretion. Thus, the dynamical state of massive dense cores needs to be measured to distinguish between the two models.

Infrared dark clouds (IRDCs), which were first identified as dark regions against the diffuse mid-infrared emission in the Galactic plane (Perault et al. 1996), are believed to harbor the early phase of massive star formation. Recent observations and stability analyses of IRDCs show that the turbulence and the thermal pressure are too weak to provide enough support against the gravity in dense clumps and dense cores (Pillai et al. 2011; Zhang et al. 2015; Ohashi et al. 2016; Sanhueza et al. 2017; Lu et al. 2018), suggesting that magnetic fields must provide significant support to bring the core to equilibrium, or that massive star formation are not in equilibrium. Thus, observational studies of the magnetic field in IRDCs are critical to address the question: does massive star formation start in equilibrium?

At a kinematic distance of $\sim$4.8 kpc, G28.34+0.06 (hereafter G28.34) is a massive ($> 10^4 M_\odot$) filamentary IRDC that harbors more than ten massive ($10^2 - 10^3 M_\odot$) molecular clumps (Carey et al. 1998; Pillai et al. 2006; Rathborne et al. 2006; Simon et al. 2006; Butler, & Tan 2009; Lin et al. 2017; Wang 2018). Three prominent clumps, MM1 (also named as P2, C9, or Dragon-Head), MM4 (also named as P1, C2, or Dragon-Belly), and MM9 (also named as S, C1, or Dragon-Tail) are revealed from millimetre (mm) dust continuum and mid-infrared extinction maps (Rathborne et al. 2006; Butler, & Tan

2009). All the three clumps are associated with water masers (Wang et al. 2006, 2008) and outflows (Wang et al. 2011; Zhang et al. 2015; Feng et al. 2016a, and this work), indicating that star formation has already began. The large gas reservoir makes them potential sites to study clustered massive star formation.

The three massive clumps are found to be in different evolutionary stages. With low temperatures (∼15 K, Wang 2018), high CO depletion (Feng et al. 2016b) and high level of deuteration (Chen et al. 2010), the 70 μm dark clump MM9 appears to be in an early stage of massive star formation. MM9 is resolved into two dense cores (C1-N and C1-S, also named as S-B and S-A, Tan et al. 2013; Feng et al. 2016b) where the south core, C1-S, further fragments into two protostellar condensations (C1-Sa and C1-Sb, Tan et al. 2016). MM4 has a temperature of ∼16 K (Wang et al. 2008) and is associated with an IR-bright protostellar source with a luminosity of 152 $L_\odot$ (Ragan et al. 2012). With high-resolution dust continuum observations, the MM4 clump is resolved into six dense cores (MM4-Core1 through MM4-Core6) along the main filament and each core further fragments into several condensations (Zhang et al. 2009; Wang et al. 2011; Zhang et al. 2015; Kong 2019a). The more energetic outflow activities, CH_3OH maser detections, less deuterium fraction, and higher luminosity in MM4 indicate that MM4 is more evolved than MM9 (Feng et al. 2019). The MM1 clump is warmer (∼30 K, Wang et al. 2008) than MM4 and MM9 and is associated with an IR-bright protostellar source with a luminosity of 2950 $L_\odot$ (Ragan et al. 2012). Previous dust continuum observations have resolved MM1 into two fragments (P2-SMA1 and P2-SMA2, Zhang et al. 2009). The rich organic molecular line emissions in P2-SMA1 indicate that it might be a hot molecular core (Zhang et al. 2009). These observations suggest that MM1 is at a later stage of massive star formation than MM4.

We present 1.3 mm Atacama Large Millimeter/submillimeter Array (ALMA) polarization observations toward clumps MM1, MM4, and MM9 in this paper. In Section 2, we summarize the observation and data reduction. In Section 3, we present maps of dust continuum, polarized dust emission, and molecular line emission, and derive the magnetic field strength. In Section 4, we discuss the dynamical state, outflow-magnetic field alignment, and fragmentation, and compare the orientations of magnetic fields, local gravity, and intensity gradient. In Section 5, we provide a summary of this paper.

2. OBSERVATION

Table 1. Source coordinates

Source	Field	α_{J2000}	δ_{J2000}
MM1	MM1	$18^h42^m52^s.06$	$-03°59'54''.3$
MM4	MM4_1	$18^h42^m51^s.05$	$-04°03'08''.6$
	MM4_2	$18^h42^m50^s.69$	$-04°03'13''.4$
	MM4_3	$18^h42^m50^s.39$	$-04°03'19''.0$
	MM4_4	$18^h42^m49^s.88$	$-04°03'24''.5$
MM9	MM9_1	$18^h42^m46^s.48$	$-04°04'14''.3$
	MM9_2	$18^h42^m46^s.91$	$-04°04'09''.3$

Figure 1 presents an overview of G28.34 in IRAM-30m 1.3mm dust continuum (Rathborne et al. 2006). The observations of three massive clumps (MM1, MM4, MM9) in G28.34 were carried out with the ALMA between 2017 Apr 18 to 2018 Jun 29 under projects 2016.1.00248.S (Cycle 4; PI: Zhang) and 2017.1.00793.S (Cycle 5; PI: Zhang). An ALMA execution on 2017 April 21 under project 2016.1.00248.S was failed due to some correlator issues and was not used for our analysis. Tables 1 and 2 list the detailed information of the observations. The total on-source time is 17 minutes for MM1 and 17 minutes (in C40-3 or C43-3 configuration) + 8 minutes (in C43-1 configuration) for each fields of MM4 and MM9. The receiver was tuned to cover frequencies ∼215.5-219.5 GHz and ∼232.5-234.5 GHz (band 6), with a total bandwidth of 5.6 GHz (three basebands, with 1.875 GHz effective bandwidth each) for the dust continuum emission in the full polarization mode. Four spectral windows in another baseband were set to cover the CO (2-1), OCS (19-18), ^{13}CS (5-4), and N_2D^+ (3-2) lines with a channel width of 122 kHz (0.16 km s^{-1}) over a bandwidth of 58.6 MHz (∼76 km s^{-1}).

The data taken in 2017 Apr 18 were manually calibrated by the authors using the Common Astronomy Software Applications (CASA, McMullin et al. 2007) and the rest of the data were calibrated by the ALMA supporting staff. The systematic flux uncertainty of ALMA at Band 6 due to calibration is ∼10 %. We performed two iterations of phase-only self-calibrations on the continuum data using the CASA. The molecular line cubes and Stokes I, Q, and U maps of dust continuum were produced from the visibility data using the CASA task *TCLEAN* with a briggs weighting parameter of robust = 0.5. The maps for MM4 and MM9 are constructed from four-pointing mosaic of MM4_1, MM4_2, MM4_3, and MM4_4, and two-pointing mosaic of MM9_1 and MM9_2, respectively. The synthesized beams of the maps are 0″.8-0″.9 × 0″.6-0″.7 (∼0.02-

Table 2. Observational parameters

Date[a]	Configuration	N_{ant}[b]	Bandpass calibrator	Gain calibrator	Flux calibrator	Pol calibrator	Sources
2017 Apr 18	C40-3	48	J1751+0939	J1851+0035	Titan	J1751+0939	MM1, MM4, MM9
2018 Apr 29	C43-3	43	J1751+0939	J1851+0035	Titan	J1751+0939	MM1, MM4, MM9
2018 Jun 23	C43-1	47	J1751+0939	J1851+0035	J1751+0939	J1924-2914	MM4, MM9
2018 Jun 29	C43-1	45	J1751+0939	J1851+0035	J1751+0939	J1924-2914	MM4, MM9

[a] Observations were under precipitable water vapor (PWV) ranging from 1.3 to 2.1 mm.

[b] Number of antennas.
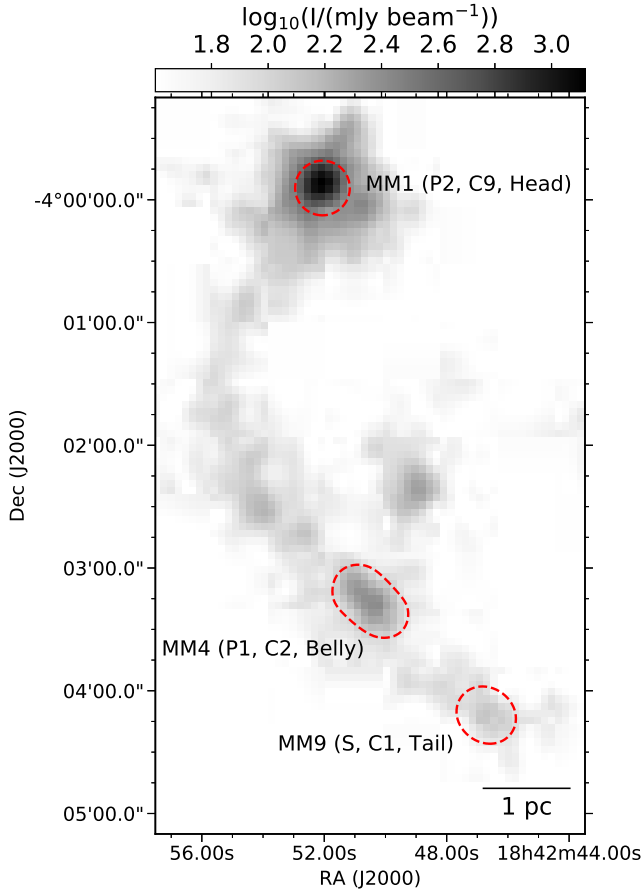
Figure 1. Overview of the IRDC G28.34 (the Dragon Nebula). The gray scale shows the IRAM-30m 1.2 mm dust continuum of G28.34 with a resolution of $11''$ (Rathborne et al. 2006). The red dashed contours indicate the Full Width at Half-Maximum (FWHM) field of view of our ALMA observations.

0.015 pc at a source distance of 4.8 kpc). The maximum

recoverable scale[2] is $\sim 7''$ (~ 0.14 pc at 4.8 kpc) for MM1 and $\sim 13''$ (~ 0.3 pc at 4.8 kpc) for MM4 and MM9. After primary beam correction, the 1σ rms noises of the Stokes I maps of dust continuum reach ~ 300, 80, and 60 μJy/beam for MM1, MM4, and MM9, respectively, while the the Stokes Q/U maps have rms noises of ~ 35 μJy/beam for MM1 and ~ 15 μJy/beam for MM4 and MM9. The sensitivity of the primary beam response corrected spectral line cubes for MM1, MM4, and MM9 is ~ 2.2, 1.2, and 1.4 mJy/beam, respectively, with a velocity channel width of 0.5 km s^{-1}.

Because the polarized intensity and polarized percentage are defined as positive values, the measured quantities of the two parameters are biased toward larger values (Vaillancourt 2006). The debiased polarized intensity PI and its corresponding uncertainty σ_{PI} are calculated as:

$$PI = \sqrt{Q^2 + U^2 - \sigma_{Q/U}^2},\qquad(1)$$

and

$$\sigma_{PI} = \sqrt{2}\sigma_{Q/U},\qquad(2)$$

where $\sigma_{Q/U}$ is the 1σ rms noise of the Q/U maps. The debiased polarization percentage P and its uncertainty δP are therefore derived by:

$$P = \frac{PI}{I},\qquad(3)$$

and

$$\delta P = \sqrt{(\frac{\sigma_{PI}^2}{I^2} + \frac{\sigma_I^2(Q^2 + U^2)}{I^4})},\qquad(4)$$

where σ_I is the 1σ rms noise of the I map.

Finally, the polarization position angle θ and its uncertainty $\delta\theta$ (Naghizadeh-Khouei & Clarke 1993) are estimated to be:

$$\theta = \frac{1}{2}\tan^{-1}(\frac{U}{Q}), \tag{5}$$

and

$$\delta\theta = \frac{1}{2}\sqrt{\frac{\sigma_{Q/U}^2}{(Q^2+U^2)}}, \tag{6}$$

3. RESULTS

3.1. Dust continuum

The 1.3 mm continuum emissions of three clumps are shown in Figure 2. In this subsection, we briefly overview the dust continuum emissions in MM4 and MM9 and focus on interpreting the dust continuum of MM1.

The MM4 region was studied by Zhang et al. (2015), Kong et al. (2018a), and Kong (2019a), which revealed six cores (MM4-Core1 to MM4-Core6 from northeast to southwest) along the natal filament and identified the condensation-scale fragment structures in the continuum emission. We adopt the condensations identified by Zhang et al. (2015) and Kong (2019a) in our study. In MM9, two massive dense cores (C1-N and C1-S) were identified by Tan et al. (2013). C1-S was further resolved into two protostellar condensations (C1-Sa and C1-Sb: Tan et al. 2016; Kong et al. 2018b). Due to sensitivity limitation, the two more candidate protostellar sources (C1a and C1b: Tan et al. 2016) away from C1-N and C1-S are not detected in our ALMA 1.3 mm continuum.

The continuum emission of MM1 is resolved down to condensation scales (see Figure 2). The emission is dominated by a major core (hereafter MM1-Core1) in the west, which further fragments into several condensation structures. Several more condensations are detected in the east and in the southwest, which are connected to the main core. Another strong condensation is seen to the northwest of the main core. There appears to be two additional 6σ continuum peaks to the northeast and to the east of MM1-Core1.

To characterize the dense structures in MM1, we applied the dendrogram (Rosolowsky et al. 2008) technique on the dust continuum using the Python package *astro-dendro*. The dendrogram abstracts the changing topology of the isosurfaces as a function of contour levels and tracks the hierarchical structure over a range of scales (Rosolowsky et al. 2008). This algorithm mainly has three parameters: the minimum value for the structure to be considered (min_value), the minimum height required for a structure to be retained as independent (min_delta), and the minimum number of pixels for a structure to be considered (min_npix). Following similar works in Cheng et al. (2018) and Liu et al. (2018), we adopt min_value $= 4\sigma$, min_delta $= 1\sigma$, and set min_npix to be the number of pixels in half beam area. We note that the combination of min_value and min_delta ensures that the identified structures have peak fluxes $> 5\sigma$.

The structures identified by dendrogram in MM1 are shown in Figure 3. The dendrogram reports the coordinates, the integrated flux ($S_{\rm int}$), the FWHM sizes along the major and minor axes, and the position angles ($\theta_{\rm dendro}$) of the structures. The parameters derived by dendrogram are reported in Table 3. The brightest two sources, Condensation 1 and Condensation 2, corresponds to P2-SMA1 and P2-SMA2 in Zhang et al. (2009). We note that nearly all condensations in MM1 are smaller than the beam area except for Condensation 8, which is marginally resolved.

With the assumptions of the optically thin dust emission, isothermal, and a **gas-to-dust ratio Λ of 100:1** (Beckwith & Sargent 1991), the gas mass M of the dense structures can be calculated with

$$M = \frac{\Lambda S_{\rm int} d^2}{\kappa_\nu B_\nu(T)}, \tag{7}$$

where $d = 4.8$ kpc is the distance to G28.34, $\kappa_\nu = (\nu/1\mathrm{THz})^\beta$ is the dust opacity (Hildebrand 1983) in m^2 kg^{-1}, and $B_\nu(T)$ is the Planck function at temperature T. Multi-wavelength observations toward massive star-forming regions usually found dust emissivity indexes β of ~ 1.5 (Beuther et al. 2007; Chen et al. 2007). Adopting this value, the κ_ν is estimated to be 0.11 m^2 kg^{-1}. The gas temperature map of the entire IRDC G28.34 was derived by Wang (2018) with combined VLA and Effelsberg 100m data (Wang et al. 2008) of the NH$_3$ (1,1) and (2,2) lines at a resolution of $6''.5 \times 3''.6$. The temperatures of the condensations in MM1 ranges from 15 K to 27 K. Considering that Condensation 1 is a hot molecular core (Zhang et al. 2009), the NH$_3$ (1,1) and (2,2) lines, which are cold gas tracers (Ho, & Townes 1983), might have underestimated the gas temperature in this condensation. As a good approximation of dust heated by a central source with luminosity L_*, the dependence of dust temperature T on radius r behaves like a simple power-law (Terebey et al. 1993):

$$T = T_0(\frac{r}{r_0})^{-q}(\frac{L_*}{L_0})^{q/2}, \tag{8}$$

where T_0 is the fiducial dust temperature at a fiducial radius r_0 from a central source with luminosity L_0 and q is the power-law index. The luminosity of the embedded protostellar object in Condensation 1 is $L_* = 2950L_\odot$
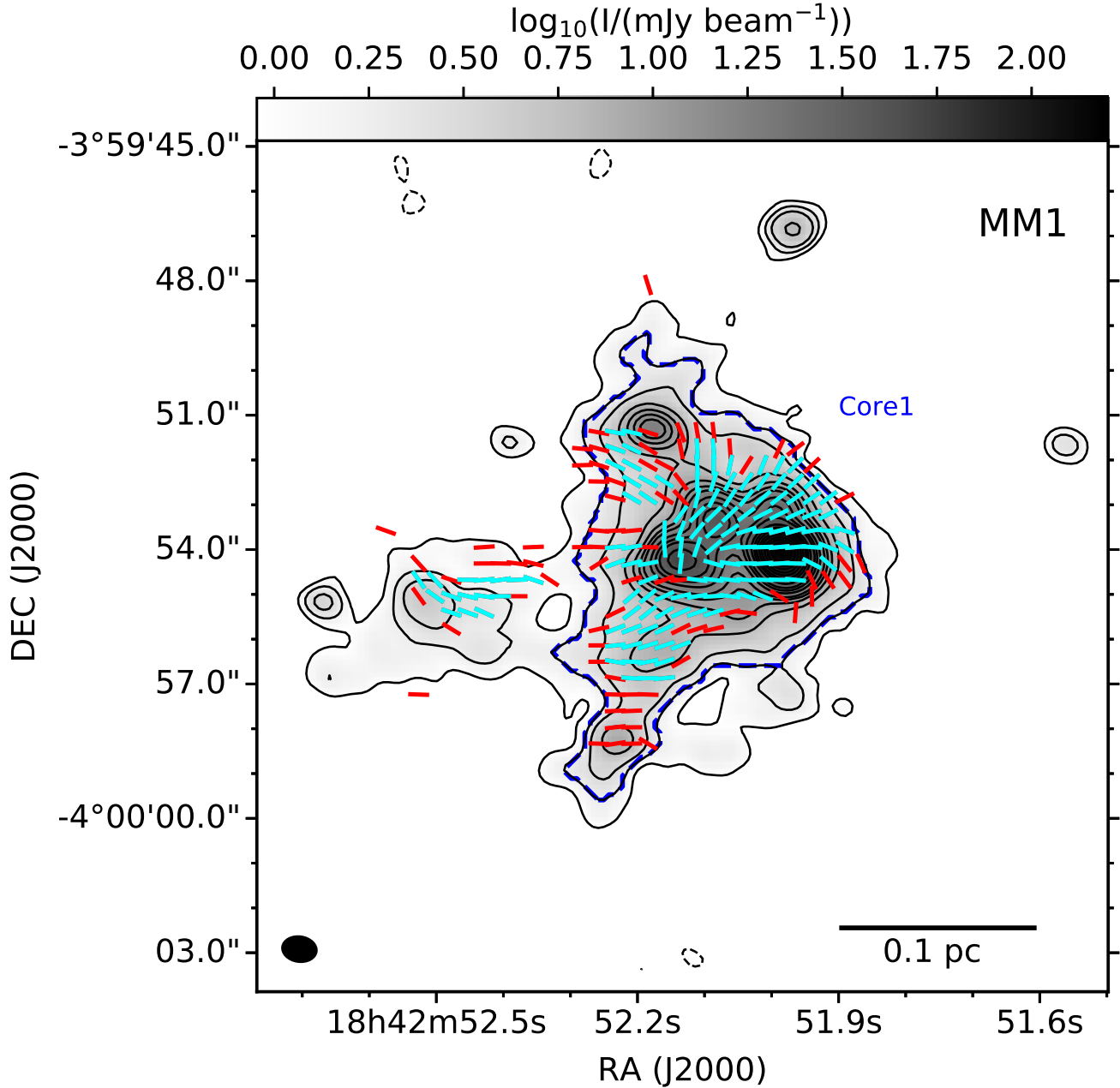
Figure 2. Dust continuum and magnetic orientation maps. The Stokes I of the ALMA 1.3 mm continuum is shown in gray scales and in contours. The ALMA 1.3 mm continuum of three clumps are also shown in contours. The contour levels are (± 3, 6, 10, 20, 30, 40, 50, 70, 90, 110, 150, 180, 210, 250, 290, 340, 390, 450) $\times \sigma_I$, where σ_I is the rms noise of the Stokes I maps (see Section 2). Line segments represent the orientation of the plane-of-sky magnetic field and have arbitrary length. Red and cyan line segments correspond to data with $PI/\sigma_{PI} > 2$ and $PI/\sigma_{PI} > 3$, respectively. Blue dashed regions indicate the areas of MM1-Core1 and MM4-Core4 in which the polarization data are used for the angular dispersion function analysis. The size of the synthesized beam are indicated in the lower left corner of each panel.
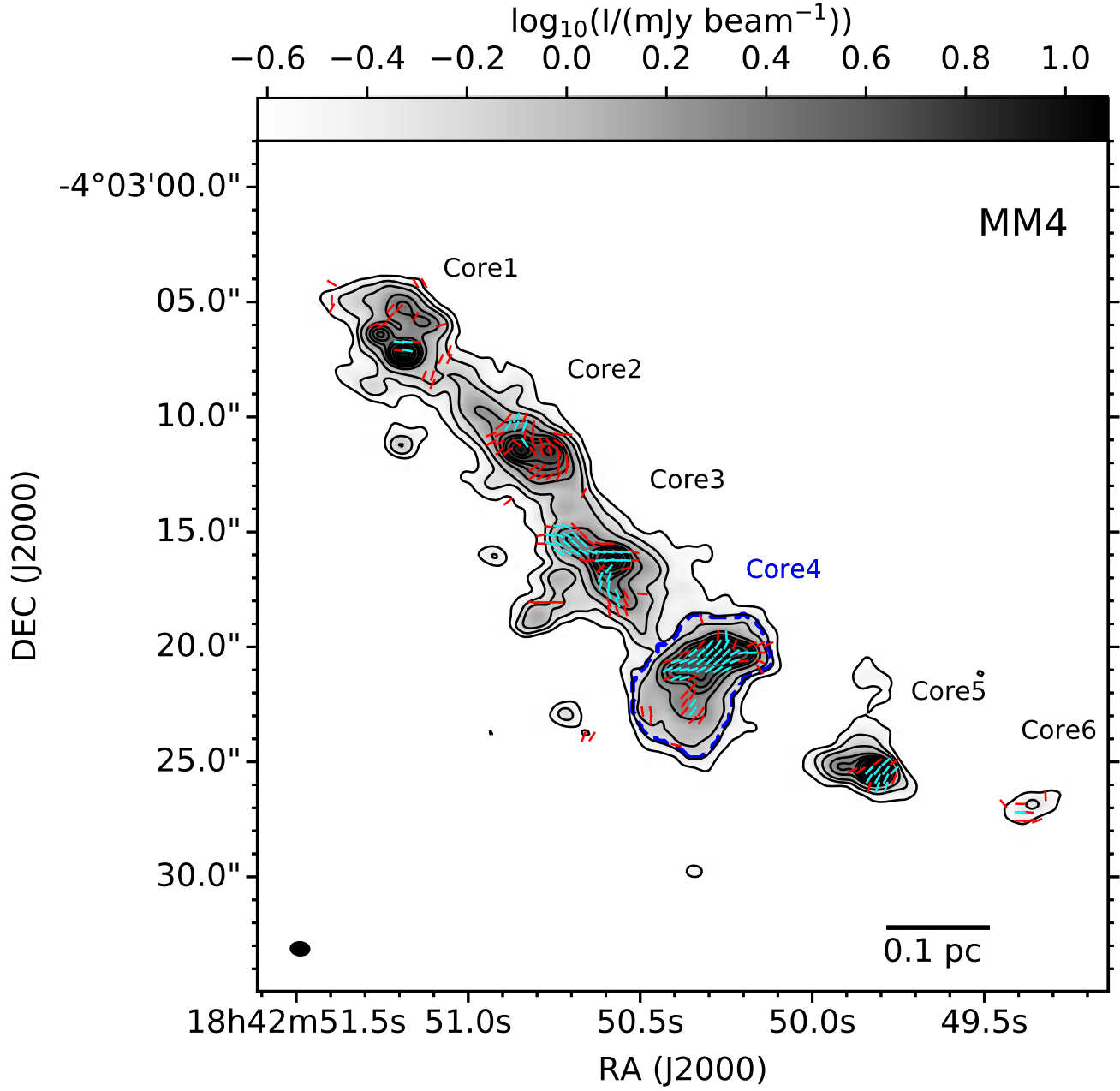
Figure 2. (Continued)
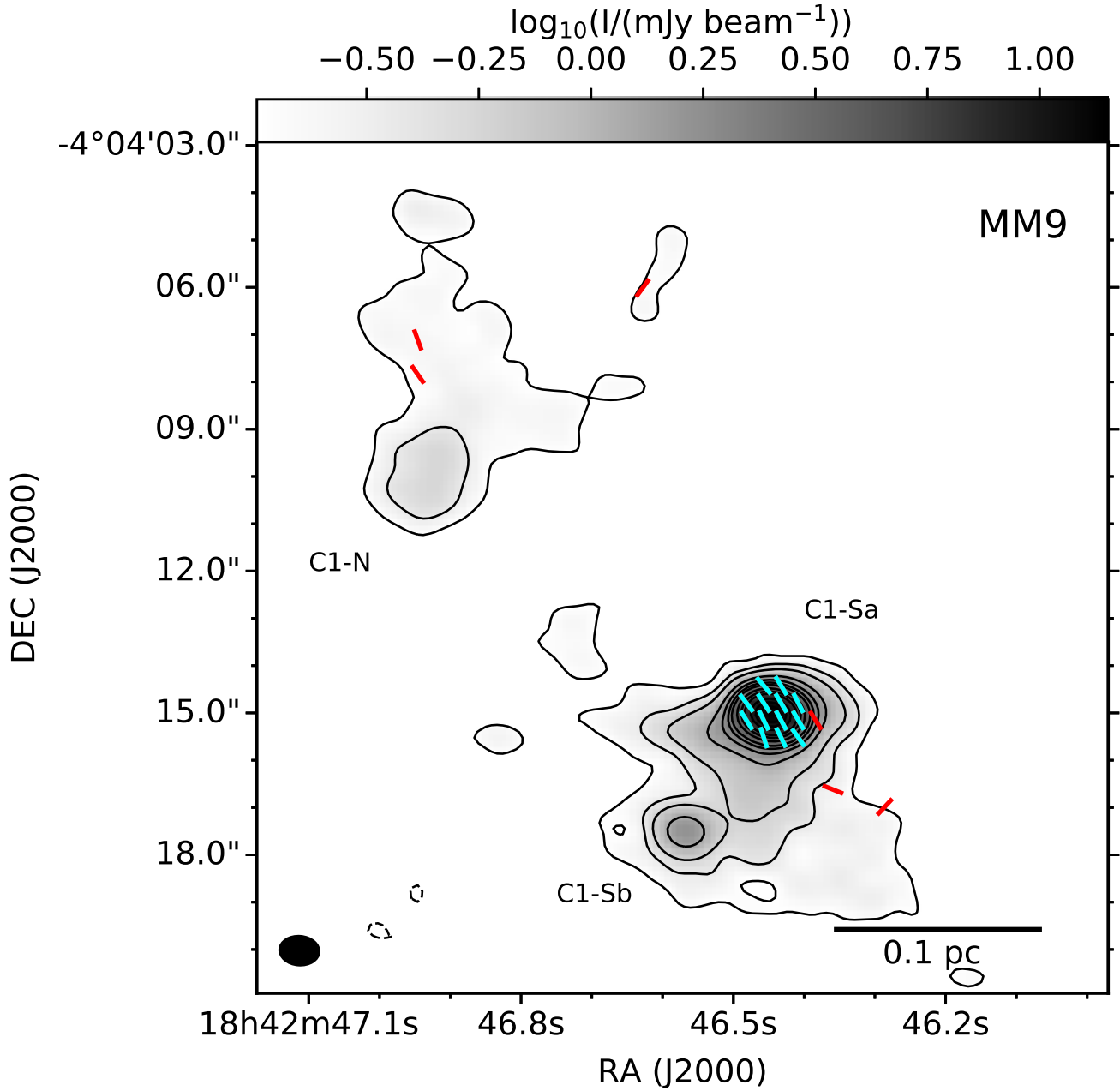
Figure 2. (Continued)

(Ragan et al. 2012). Adopting $T_0 = 38$ K, $r_0 = 100$ AU, $L_0 = 1$ $L_\odot$, $q = 0.4$ (Motte & André 2001), and a background temperature of 20 K (Wang 2018), the average temperature of Condensation 1 within a radius of mean FWHM (FWHM$_{mean}$) is measured to be 57.0 K. A temperature of 30 K (Wang et al. 2008) is adopted for MM1-Core1. With a similar approach and adopting a temperature of $\sim$16 K (Wang et al. 2008), we also derived the mass for MM4-Core4. The estimated masses and temperatures are listed in Table 3.

The average column density N_{H_2} and volume density n_{H_2} within each core and condensation are measured using a radius equal to the FWHM$_{mean}$:

$$N_{H_2} = \frac{M}{\mu_{H_2} m_H \pi \text{FWHM}_{mean}^2}, \qquad (9)$$

$$n_{H_2} = \frac{3M}{4\mu_{H_2} m_H \pi \text{FWHM}_{mean}^3}, \qquad (10)$$

where $\mu_{H_2} = 2.86$ is the mean molecular weight per hydrogen molecule (Kirk et al. 2013; Pattle et al. 2015)

Table 3. Physical parameters of dense structures

Source	RA	DEC	$S_{\rm int}$[a]	FWHM[b]	$\theta_{\rm dendro}$	T	M	$N_{\rm H_2}$	$n_{\rm H_2}$
	(h:m:s)	(d:m:s)	(mJy)	$'' \times ''$	(°)	(K)	($M_\odot$)	(10^{23} cm^{-2})	(10^6 cm^{-3})
MM1-Core1	18:42:52.06	-3:59:54.04	745.4	2.8×2.6	-138.8	30.0	212.4	5.0	3.2
Condensation 1	18:42:51.98	-3:59:54.06	258.0	0.8×0.6	126.2	57.0	35.5	>13.6	>29.2
Condensation 2	18:42:52.12	-3:59:54.23	57.7	0.6×0.4	177.8	23.6	21.9	>23.5	>56.5
Condensation 3	18:42:52.08	-3:59:53.41	25.0	0.4×0.3	97.0	23.6	9.5	>20.4	>65.6
Condensation 4	18:42:52.17	-3:59:51.35	26.8	0.7×0.5	159.5	24.1	9.9	>5.7	>11.8
Condensation 5	18:42:52.2	-3:59:58.24	9.7	0.6×0.5	53.9	17.3	5.5	>4.7	>11.0
Condensation 6	18:42:52.16	-3:59:56.16	9.8	0.7×0.4	-148.4	23.6	3.7	>4.0	>8.8
Condensation 7	18:42:51.96	-3:59:46.8	7.0	0.6×0.5	-155.7	15.2	4.7	>3.2	>8.8
Condensation 8	18:42:52.49	-3:59:55.26	12.2	1.1×0.7	170.7	21.9	5.1	>1.9	>2.5
Condensation 9	18:42:52.66	-3:59:55.19	2.8	0.5×0.4	156.2	17.7	1.6	>1.8	>5.2
Condensation 10	18:42:51.98	-3:59:57.14	2.2	0.5×0.4	149.3	26.4	0.7	>1.1	>2.8
Condensation 11	18:42:51.56	-3:59:51.66	1.5	0.4×0.3	154.8	20.2	0.7	>1.2	>4.2
Condensation 12	18:42:52.43	-3:59:56.17	1.4	0.4×0.3	158.5	19.4	0.7	>1.6	>5.4
Condensation 13	18:42:52.38	-3:59:51.5	0.9	0.4×0.3	161.6	19.8	0.4	>1.1	>4.2
Condensation 14	18:42:52.64	-3:59:56.81	1.2	0.6×0.2	179.3	17.7	0.6	>1.3	>3.9
Condensation 15	18:42:52.08	-3:59:58.52	1.7	0.7×0.3	176.0	21.1	0.7	>1.0	>2.6
MM4-Core4	18:42:50.31	-4:03:21.07	68.3	2.9×1.8	45.9	16.0	43.0	1.5	1.1

[a]Integrated flux.

[b]Without deconvolution.

and $m_{\rm H}$ is the atomic mass of hydrogen. The derived column and volumn densities are also listed in Table 3. The estimated $n_{\rm H_2}$ and $N_{\rm H_2}$ of the condensations in MM1 and the two cores are generally comparable to those in other IRDCs and in more evolved massive star-forming regions ($n_{\rm H_2} \sim 10^5$-10^7 cm^{-3} and $N_{\rm H_2} \sim 10^{22}$-10^{24} cm^{-2}. e.g., Liu et al. 2018; Lu et al. 2018; Cao et al. 2019; Sanhueza et al. 2019). The main uncertainty of the calculations comes from the uncertainty of κ_ν (Henning et al. 1995). We conservatively adopt a fractional uncertainty of 50% (Roy et al. 2014) for M, $N_{\rm H_2}$, and $n_{\rm H_2}$. We note that since most condensations are unresolved, the derived $N_{\rm H_2}$ and $n_{\rm H_2}$ for these condensations should be regarded as lower limits.

3.2. *Polarized emission of dust*

The plane-of-sky magnetic field orientation can by derived by rotating the orientation of the observed linear dust polarization of the electric field by 90° with the assumption that the shortest axis of dust grains is perfectly aligned with the magnetic field. Figure 2 shows the inferred magnetic field orientations overlaid on the Stokes I maps toward the massive clumps MM1, MM4, and MM9. The ALMA maps reveal compact structures

in the clumps down to scales of $\sim$0.02 pc (condensation scale).

The magnetic field structure in MM1 is well resolved and shows a radial pattern, indicating that the field might be dragged towards the center by gravity. We further compare the magnetic field with the local gravity in Section 3.6.

In MM4, strong polarized emissions are detected in MM4-Core3, MM4-Core4, and MM4-Core5, while the polarized emissions in MM4-Core1, MM4-Core2, and MM4-Core6 are only marginally detected. The polarized emission in Core5 is compact and centered at the continuum peak in the west of the core, showing a northwest-southeast orientated magnetic field that is orthogonal to the parent filament. The polarized emission in MM4-Core4 is the most extended in MM4 and the magnetic field in the northern part of this core is well resolved, while the magnetic field in the southern part is only partially resolved. Similar to Core5, the magnetic field in Core4 shows a northwest-southeast orientation. The magnetic field in Core3 can be divided into three groups: the magnetic field in the center shows a east-west orientation; the magnetic field in the northeastern part shows a northeast-southwest orientation; and the mag-
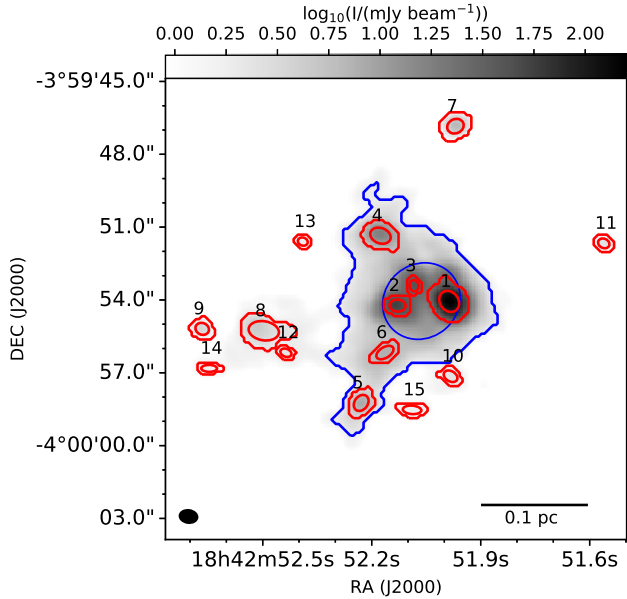
Figure 3. Structures identified by dendrogram in MM1. The gray scale shows the 1.3 mm continuum emission. Red and blue contours indicate the boundries of the identified leaves (i.e., condensations) and MM1-Core1, respectively. Red and blue ellipses indicate the FWHM and position angle of the condensations and MM1-Core1, respectively, computed by dendrogram.

netic field in the southern part rotates smoothly, showing a C-shaped morphology.

In MM9, the polarized emission is confined at the continuum peak (C1-Sa) and the magnetic field shows a northeast-southwest orientation, following the parent filament.

In Figure 4, we show contours of the polarization emission intensity overlaid on the polarization percentage maps. In Figure 5, the P-I relation in the three clumps is shown. The polarization percentage is detected down to 0.3%, 0.8%, and 1.3% in MM1, MM4, and MM9, respectively. Clear trends of decreasing P with increasing I are seen in MM1 and MM4. For the P-I relations in MM1 and MM4, the polarization percentage at a constant I shows broad scatters up to a order of magnitude, which indicates that the depolarization seen in the two clumps are the combined results of different factors. Using χ^2 minimization, we fit the P-I anti-correlations in MM1 and MM4 where $P/\delta P > 3$ with a simple power-law $P \propto I^\alpha$ and the power-law slope index α is estimated to be approximately -0.3 and -0.7 for MM1 and MM4, respectively. Due to the large scattering in the P-I relations, we refrain from interpreting the absolute value of the slope indexes. However, we notice that the P-I relation in MM1 is shallower than that in MM4, which may suggest the grain alignment efficiency is improved
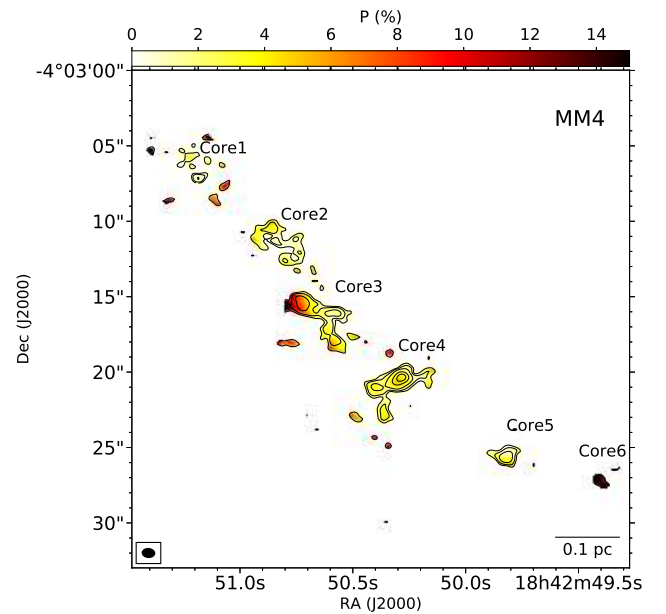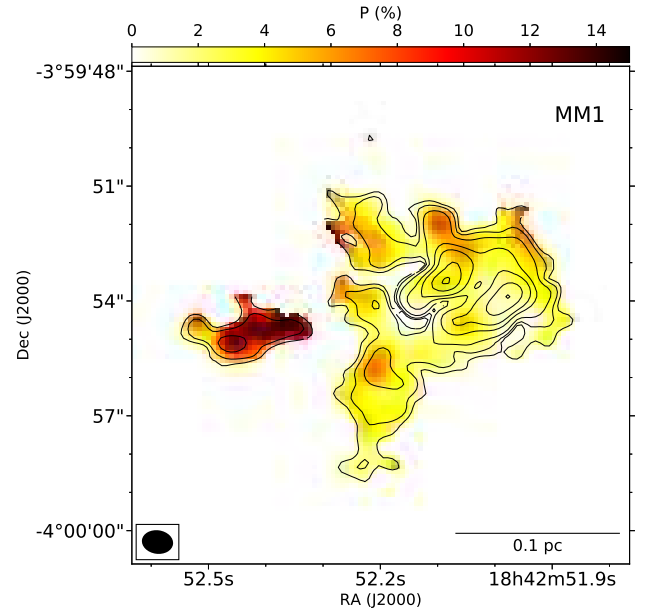
Figure 4. Dust polarization maps. The polarization percentage is shown in color scales. Black solid contours show the polarized intensity. Contour levels are (2, 3, 5, 10, 15, 25, 35, 50) $\times \sigma_{PI}$, where σ_{PI} is the rms noise of the polarized intensity ($\sim$50 μJy/beam for MM1 and $\sim$20 μJy/beam for MM4 and MM9).
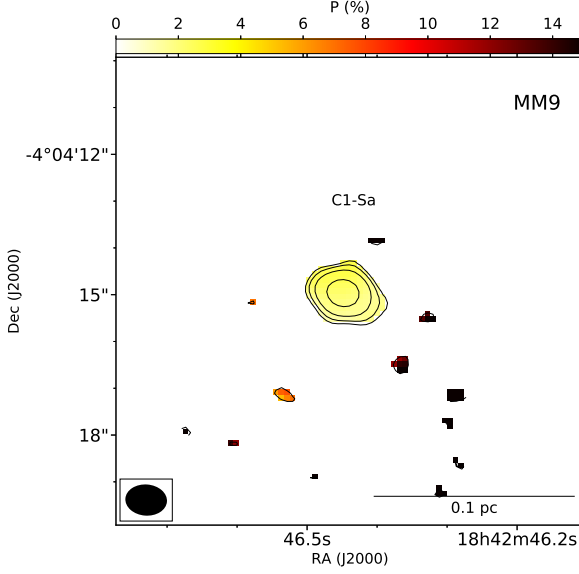
Figure 4. (Continued)

by additional internal radiation in more evolved star formation regions. Similar trend of shallower P-I relation in more evolved cores is also seen in the low-mass star formation dense cores in the Ophiuchus cloud (Kwon et al. 2018; Soam et al. 2018; Liu et al. 2019; Pattle et al. 2019). In MM9, the polarized percentages is $\sim$2%.

3.3. Molecular lines

Figure 6 show the zeroth-moment maps of N_2D^+ (3-2), ^{13}CS (5-4), and OCS (19-18) in MM1, MM4, and MM9. The line emissions in three clumps share some similar patterns. The ^{13}CS and OCS lines show similar emission morphology and present the strongest emission mostly near the dust continuum peaks. The distribution of the N_2D^+ emision is almost anti-correlated with that of the ^{13}CS and OCS emission, indicating that the ^{13}CS and OCS molecules are likely depleted in the cold and dense gas highlighted by the N_2D^+ emision.

In MM1, the emissions from ^{13}CS and OCS peak at Condensation 1. The N_2D^+ line shows strong emissions to the north of Core1, which appears to be extended and probably links Condensation 7 with MM1-Core1. There are also faint N_2D^+ emissions in Condensation 10 and between Condensations 5 and 6. The lack of N_2D^+ detection in the dust emission region indicates that MM1 is in a later evolution stage of star formation.

In MM4, the N_2D^+ emission is detected in MM4-Core1 through Core5, while the ^{13}CS and OCS emissions are detected in MM4-Core1 through Core4. The line emission of three molecules are mostly overlapping with dust continuum emissions, except that there appears to be an N_2D^+ emission peak to the east of MM4-Core1
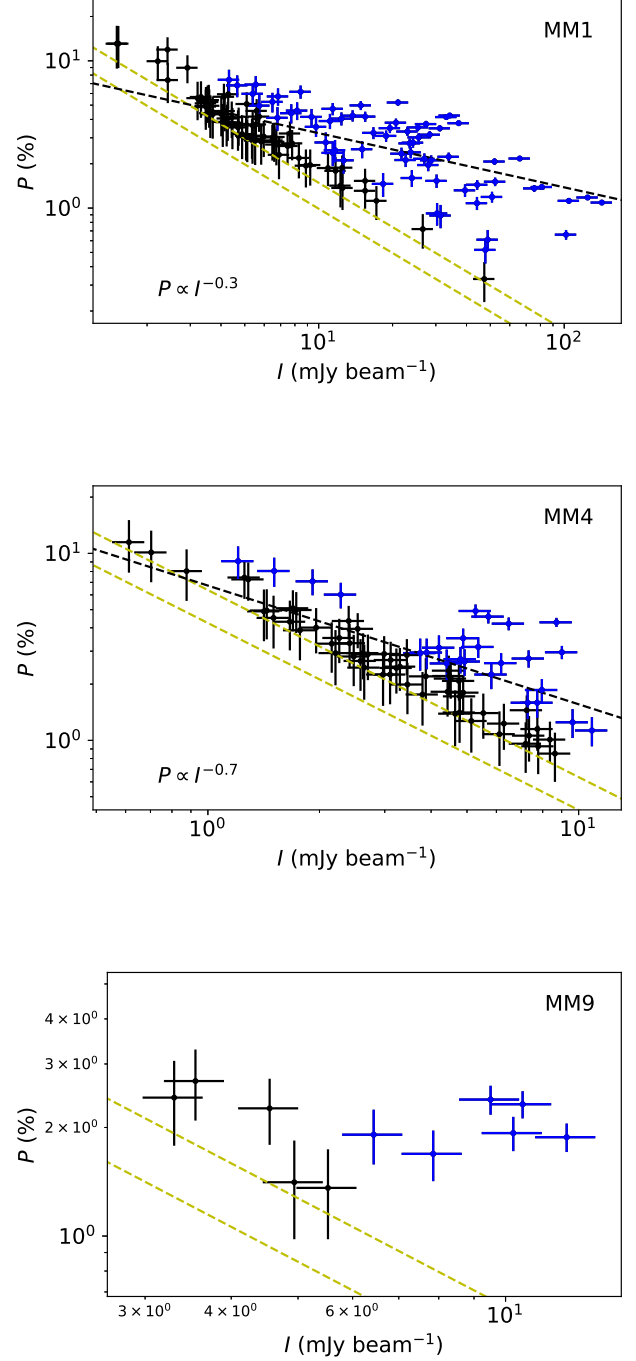

Figure 5. Polarization percentage vs. Stokes I. Data points with $P/\delta P > 3$ and $P/\delta P > 5$ are shown with error bars in black and blue colors, respectively. Yellow dashed lines show the $2\sigma_{PI}$ and $3\sigma_{PI}$ noise levels. Results of the power-law fit for data with $P/\delta P > 3$ are shown in black dashed lines.

and an OCS emission peak to the south of MM4-Core1, which are not associated with the dust emission above 3σ. The ^{13}CS and N$_2$D$^+$ maps generally agree with previous observations reported in Zhang et al. (2015), but show improvements in detecting fainter and more extended emissions.

In MM9, the ^{13}CS and OCS emissions are only marginally detected in C1-S. The N$_2$D$^+$ emission in core C1-S are consistent with previous observations (Tan et al. 2013, 2016; Kong et al. 2018b). Due to the limitation of sensitivity, the N$_2$D$^+$ emission in core C1-N is only marginally detected.

3.4. *Molecular outflows in MM1*

The molecular outflows in MM4 (Wang et al. 2011; Zhang et al. 2015) and MM9 (Feng et al. 2016a; Tan et al. 2016; Kong et al. 2018b) have been widely studied, so we only present the outflows of MM1 in CO (2-1) in this paper (see Figure 7). The outflow emissions in MM1 are detected throughout the velocity coverage of our observations ($\sim$41 km s^{-1} to $\sim$116 km s^{-1}). Figure 7(a) shows the integrated emissions of CO in velocity ranges from 45 km s^{-1} to 74 km s^{-1} for the blue-shifted lobe, and 84 km s^{-1} to 115 km s^{-1} for the red-shifted lobe. The data channels with velocities <84 km s^{-1} and >74 km s^{-1} are excluded in the integration to avoid the contamination of surrounding diffuse gas. We also excluded channels with velocities <45 km s^{-1} or >115 km s^{-1} in the integration due to domination of instrumental noise in these edge channels. Figure 7(b) shows the integrated emission of the high-velocity (HV) outflow gas with velocities >20 km s^{-1} with respect to MM1's ambient velocity. The outflows in MM1 show clustered overlapping structures. The HV outflow components are highly collimated and show some jet-like structures. Due to the complex structure of the outflows and the lack of shock tracers (e.g., SiO) to trace the vicinity outflow gas, we refrain from detailed analysis of the MM1 outflow and leave it to future studies.

3.5. *Magnetic field strength of MM1-Core1 and MM4-Core4*

The Davis-Chandrasekhar-Fermi (DCF; Davis 1951; Chandrasekhar & Fermi 1953) method and its modified form have been widely used to estimate the plane-of-sky magnetic field strength (B_{pos}) by interpreting the observed angular dispersion ($\Delta\theta$) of polarization position angles as a MHD-wave component of the field perturbed by turbulent motions. With the small angle approximation, the B_{pos} is estimated as (Crutcher et al. 2004):

$$B_{\mathrm{pos}} = Q_c\sqrt{\mu_0\rho}\frac{\sigma_{\mathrm{turb}}}{\Delta\theta} \qquad (11)$$

in SI units or CGS units, where μ_0 is the permeability of vacuum, $\rho = \mu_{\mathrm{H}_2}m_{\mathrm{H}}n_{\mathrm{H}_2}$ is the density of the gas, σ_{turb} is the line-of-sight non-thermal velocity dispersion, and Q_c is a correction factor.

Further approaches have been made on modifying the DCF method toward more accurately quantifying the angular dispersion in the DCF formula through the angular dispersion function (ADF) analysis (Falceta-Gonçalves et al. 2008; Hildebrand et al. 2009; Houde et al. 2009, 2016) or the unsharp masking analysis (Pattle et al. 2017). Specifically, Houde et al. (2016) derived the ADF for polarimetric images obtained from an interferometer, taking into account variations in the large-scale magnetic field, the effects of signal integration along the line of sight and within the beam, and the large-scale filtering effect of interferometers. The ADF is given by (Houde et al. 2016):

$$1 - \langle\cos[\Delta\Phi(l)]\rangle = \sum_{j=1}^{\infty} a_{2j}l^{2j} + \left[\frac{N}{1 + N\langle B_0^2\rangle/\langle B_t^2\rangle}\right]$$
$$\times\left\{\frac{1}{N_1}\left[1 - e^{-l^2/2(\delta^2 + 2W_1^2)}\right]\right.$$
$$+ \frac{1}{N_2}\left[1 - e^{-l^2/2(\delta^2 + 2W_2^2)}\right]$$
$$\left. - \frac{2}{N_{12}}\left[1 - e^{-l^2/2(\delta^2 + W_1^2 + W_2^2)}\right]\right\},$$
$$(12)$$

where $\Delta\Phi(l)$ is the angular difference of two line segments separated by a distance l, δ is the turbulent correlation length, the summation is the Taylor expansion of the ordered component of the ADF, B_t is the turbulent component of the magnetic field, B_0 is the ordered magnetic field, W_1 and W_2 are the standard deviation of the two Gaussian profiles of the synthesized beam and the large-scale filtering effect (i.e., the FWHM divided by $\sqrt{8\ln 2}$), and N is the number of turbulent cells probed by the telescope beam given by:
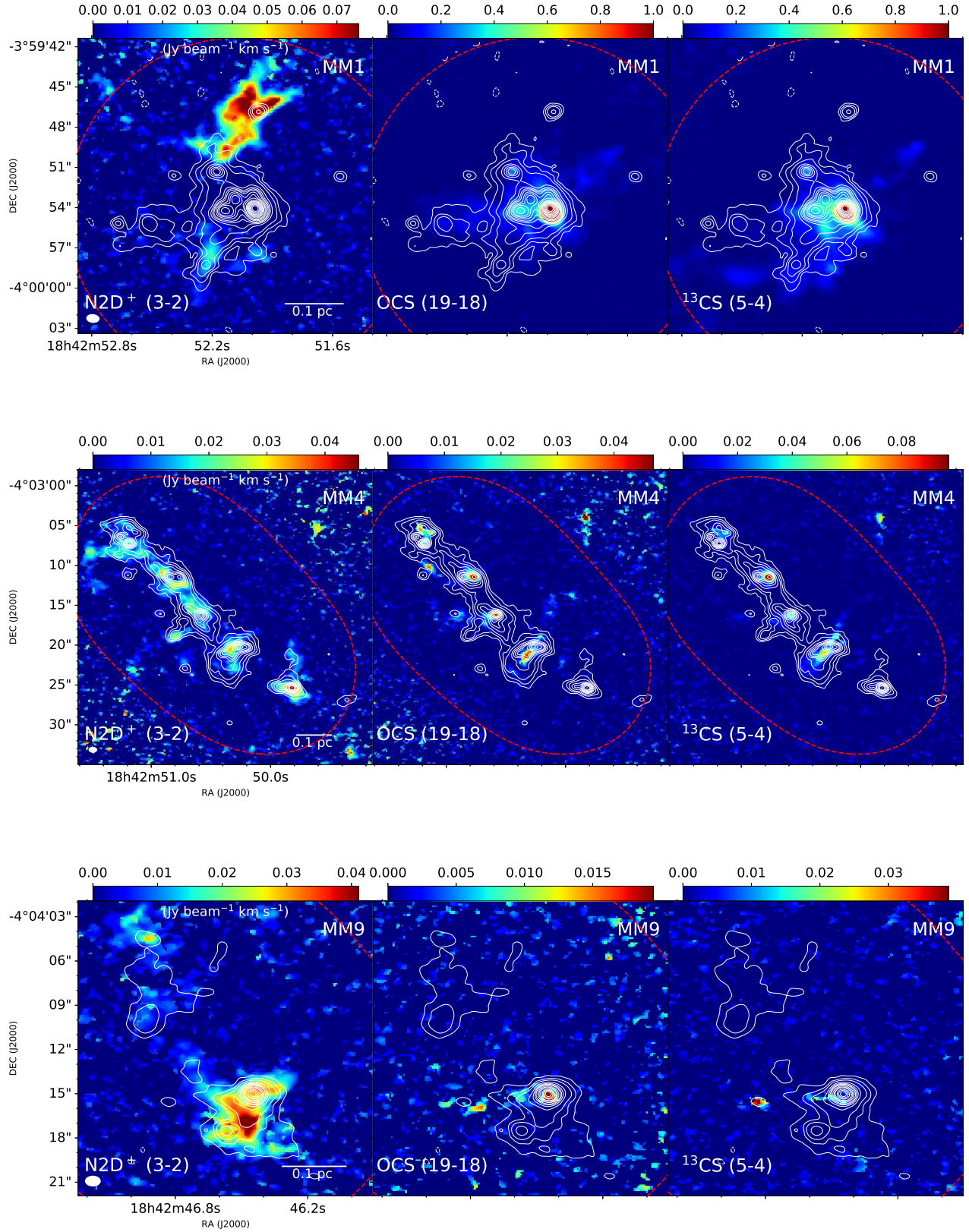
$$N_1 = \frac{(\delta^2 + 2W_1^2)\Delta'}{\sqrt{2\pi}\delta^3}, \qquad (13)$$

$$N_2 = \frac{(\delta^2 + 2W_2^2)\Delta'}{\sqrt{2\pi}\delta^3}, \qquad (14)$$

$$N_{12} = \frac{(\delta^2 + W_1^2 + W_2^2)\Delta'}{\sqrt{2\pi}\delta^3}, \qquad (15)$$

$$N = \left(\frac{1}{N_1} + \frac{1}{N_2} - \frac{2}{N_{12}}\right)^{-1}, \qquad (16)$$

where Δ' is the effective thickness of the concerned region through which the signals are integrated along the

Figure 6. Momemt 0 maps of molecular lines from N_2D^+ (3-2), ^{13}CS (5-4), and OCS (19-18) are shown in color scales. Only velocities with detection greater than 2σ rms noise are integrated. White contour levels are the same as the contour levels in Figure 2. Red contours correspond to the FWHM field of view of the ALMA observations.

(a)

(b)
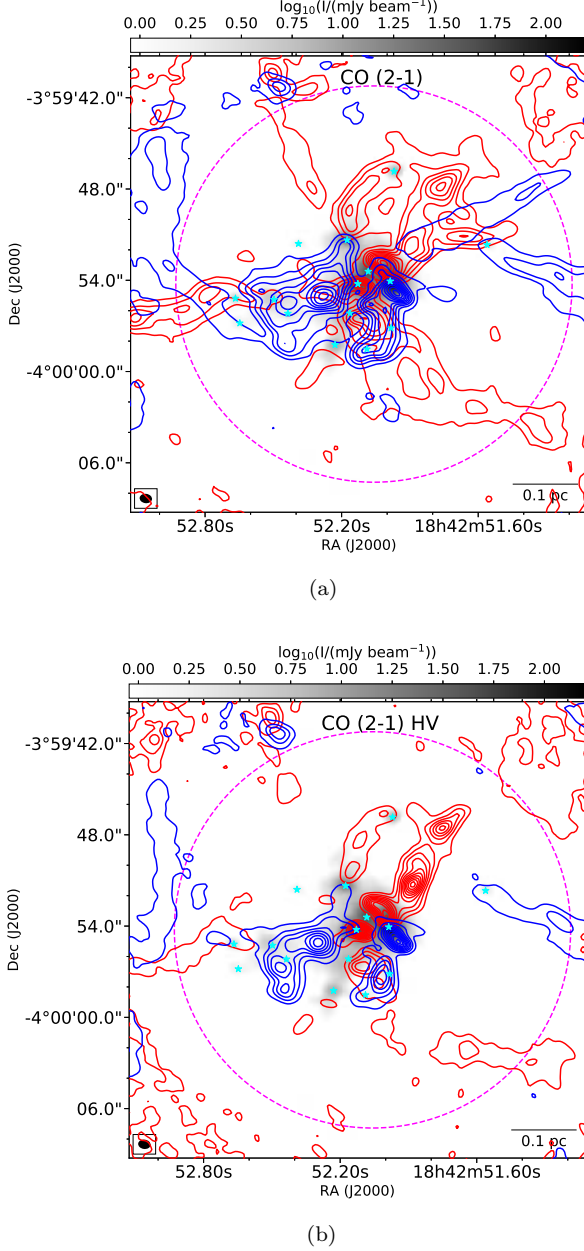
Figure 7. Molecular outflows detected in CO (2-1) in MM1. The blueshifted and redshifted outflows are shown in blue and red contours, respectively. Contour levels start from 5% and continue at 10% of the peak of the integrated CO emission. The dust continuum is shown in gray scales. Star symbols denote the position of the condensations identified by dendrogram. Magenta contours correspond to the the the FWHM field of view of the ALMA observations. (a) CO emissions integrated from 45 to 74 km s^{-1} for the blue robe, and 84 to 115 km s^{-1} for the red robe. (b) High-velocity (outflow velocity $> \pm 20$ km s^{-1}) CO emissions integrated from 45 to 59 km s^{-1} for the blue robe, and 99 to 115 km s^{-1} for the red robe.

line of sight. The turbulent component of the ADF is

$$
b^2(l) = \left[\frac{N}{1 + N\langle B_0^2\rangle/\langle B_t^2\rangle}\right] \times \left[\frac{1}{N_1}e^{-l^2/2(\delta^2 + 2W_1^2)}\right.
$$
$$
\left. + \frac{1}{N_2}e^{-l^2/2(\delta^2 + 2W_2^2)} - \frac{2}{N_{12}}e^{-l^2/2(\delta^2 + W_1^2 + W_2^2)}\right],
$$

The ordered magnetic field strength can be derived by (Houde et al. 2009):

$$
B_0 \simeq \sqrt{\mu_0\rho}\,\sigma_{\rm turb}\left[\frac{\langle B_t^2\rangle}{\langle B_0^2\rangle}\right]^{-1/2} \tag{17}
$$

in SI units or CGS units.

The Δ' is estimated as the width at half of the maximum of the normalized auto-correlation function of the integrated normalized polarized flux (Houde et al. 2009). The Δ' of MM1-Core1 and MM4-Core4 are estimated to be $2''.5$ and $2''.2$, respectively, which are consistent with the FWHMs derived from dendrogram.

The information about the nonthermal (turbulent) velocity dispersion ($\sigma_{\rm turb}$) of the gas, which is required to calculate the $B_{\rm pos}$, is determined from previous NH$_3$ observations. The line-of-sight velocity dispersions of NH$_3$ ($\sigma_{\rm NH_3}$) for MM1-Core1 and MM4-Core4 are 1.4 km s^{-1} (Wang et al. 2008) and 0.47 km s^{-1} (Wang et al. 2012), respectively. The $\sigma_{\rm turb}$ is calculated with the relation

$$
\sigma_{\rm turb}^2 = \sigma_{\rm NH_3}^2 - \frac{k_{\rm B}T}{m_{\rm NH_3}}, \tag{18}
$$

where $m_{\rm NH_3}$ is the mass of the NH$_3$ molecule. The nonthermal velocity dispersions are estimated to be 1.4 km s^{-1} and 0.46 km s^{-1} for MM1-Core1 and MM4-Core4, respectively. The corresponding 3D turbulent velocity dispersion $\sigma_{\rm turb,3D} = \sqrt{3}\sigma_{\rm turb}$ are 2.42 km s^{-1} and 0.80 km s^{-1} for MM1-Core1 and MM4-Core4, respectively.

Figures 8 and 9 show the angular dispersion functions and the turbulent component of the ADF derived from the polarization segments with $PI/\sigma_{PI} > 3$ in MM1-Core1 and MM4-Core4 (see Figure 2), respectively. To avoid large uncertainties due to sparse sampling at large spatial scales (see Appendix of Liu et al. 2019), we fit the ADFs of MM1-Core1 and MM4-Core4 over $l < 2.6''$ and $l < 3.4''$, respectively, where the angular dispersion function is relatively smooth and shows well-correlated relations with l. The best fit is obtained via χ^2 minimization. The $B_{\rm pos}$ for MM1-Core1 and MM4-Core4 are calculated to be 1.6 mG and 0.32 mG, respectively. The parameters derived from the ADF method are listed in Table 4. We note that since the polarization observations in MM4-Core4 only cover part of this core, an assumption of constant turbulent-to-ordered magnetic field ratio in the core needs to be adopted. According to

Table 4. Physical parameters relevant to the ADF analysis

Source	n_{H_2}	σ_{turb}	$(\langle B_t^2\rangle/\langle B_0^2\rangle)^{\frac{1}{2}}$	B_{pos}	δ	N	$Q_c'{}^a$
	(10^6 cm^{-3})	(km s^{-1})		(mG)	$('')$		
MM1-Core1	3.2	1.4	1.2	1.6	0.53	4.1	0.50
MM4-Core4	1.1	0.46	1.2	0.32	0.38	6.9	0.38

[a]Equivalent correction factor $Q_c' = 1/\sqrt{N}$ for the signal-integration effect.

Houde et al. (2016), the B_{pos} estimated from the ADF method is accurate within a factor of $\sim$3.

Since the line-of-sight component of the magnetic field is unknown, the 3D mean ordered magnetic field strength B is calculated with the statistical relation $B = 4B_{pos}/\pi$ (Crutcher et al. 2004). Then the 3D Alfvén velocity is estimated as

$$V_{A,3D} = \frac{B}{\sqrt{\mu_0\rho}} \tag{19}$$

in SI units or CGS units. The $V_{A,3D}$ for MM1-Core1 and MM4-Core4 are 1.5 km s^{-1} and 0.51 km s^{-1}, respectively. The Alfvén Mach number $Mach_A = \sigma_{turb,3D}/V_{A,3D}$ of MM1-Core1 and MM4-Core4 are estimated to be 1.61 and 1.57, respectively, which means that the two cores are in super-Alfvénic states (weakly magnetized)

3.6. Comparison of orientations of magnetic field, intensity gradient, and local gravity

Star-forming regions are subject to various forces such as gravity, gas pressure, magnetic force, and other possible forces. Koch et al. (2012) has used ideal magnetohydrodynamics (MHD) force equations to describe the interaction of the forces and developed a technique (the polarization-intensity gradient-local gravity method, hereafter the PIL method) to measure the local magnetic field strength. In this method, the gradient of intensity is assumed to trace the resulting direction of particle motion in the MHD force equation. Following the approach of the PIL method, we calculate the angular differences among the magnetic field, the intensity gradient (IG), and the local gravity (LG), and study the relative importance of the magnetic field and local gravity at different positions.

The surrounding mass distribution needs to be taken into account when calculating the local gravitational force at a given position in a map (Koch et al. 2012). Adopting constant temperatures for MM4 and MM9, and adopting the previously mentioned temperature profile (see section 3.1) for MM1, we derived the gas mass (m_i) for each pixel of the map with $I > 3\sigma_I$ for

the three clumps using Equation 7. The local gravity force at position r_j is then given by

$$g_j(r) = G\sum_{i=1}^n \frac{m_i m_j}{|r_j - r_i|^2}e_{ij}, \tag{20}$$

where e_{ij} is the unit vector indicating the direction between position r_i and r_j. The orientations of the local gravity force (θ_{LG}) of the three clumps are presented in Figure 10. The local gravity orientation maps show similar radial patterns toward local emission peaks, which is quite reasonable because the emission centers contain more mass and have larger gravitational potential.

3.6.1. Intensity gradient versus local gravity

The angle ψ measures the angular difference between the position angles of the intensity gradient (θ_{IG}) and that of the local gravity (θ_{LG}). Figure 11 shows the ψ maps for the three clumps. The average values of ψ in MM1, MM4, and MM9 are 30°, 22°, and 28°, respectively. The small average value of ψ indicates that the intensity gradient tend to be aligned with the local gravity and that the gravity plays an important role in regulating the gas motion. On the other hand, there seems to be large ψ values near some condensations where accretion or rotation are likely ongoing.

#### 3.6.2. Magnetic field versus intensity gradient

The angle δ measures the angular difference between the position angles of the intensity gradient (θ_{IG}) and that of the magnetic field (θ_B). Figure 12 shows the δ maps for MM1 and MM4. The average values of δ in MM1 and MM4 are 40° and 46°, respectively. The intermediate average values of δ suggests that the magnetic field plays a moderate role in resisting the gas collapse.

3.6.3. Magnetic field versus local gravity

The angle ω measures the angular difference between the position angles of the local gravity (θ_{LG}) and that of the magnetic field (θ_B). Figure 13 shows the ω maps for MM1 and MM4. The average values of ω in MM1 and MM4 are 34° and 36°, respectively. In both MM1
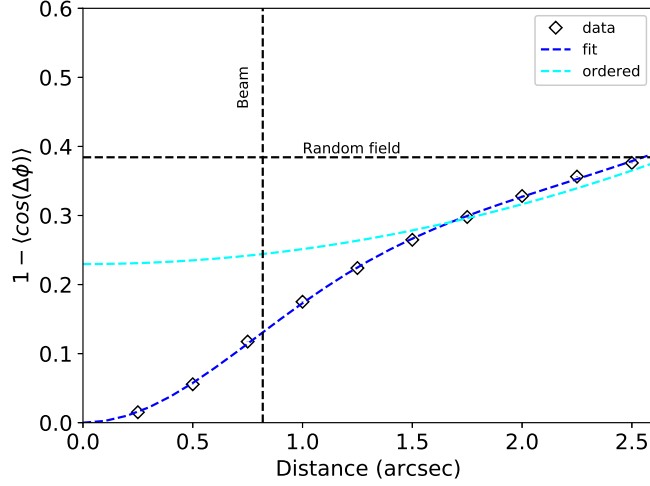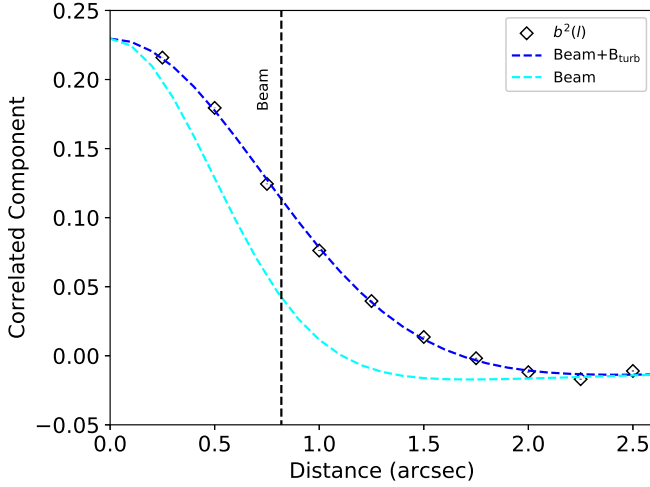
Figure 8. (a) Angular dispersion function for MM1-Core1. The angle dispersion segments are shown in diamond symbols with error bars. The error bars indicate the statistical uncertainties of the angular dispersion function propagated from the observational uncertainty. The blue dashed line shows the fitted ADF. The cyan dashed line shows the large-scale component $(1 - \langle \cos[\Delta\Phi(l)] \rangle - b^2(l))$ of the best fit. The horizonal dashed line indicates the value corresponding to a random field. (b) Correlated component $(b^2(l))$ of the ADF. The correlated component of the best fit is shown in the blue dashed line. The correlated component solely due to the beam is shown in the cyan dashed line.

and MM4, the magnetic field and the local gravity are apparently poorly aligned toward the brightest emission peaks, which might be a result of field tangling of complex small scale magnetic field along the line of sight or the perturbation from rotation and accretion. In
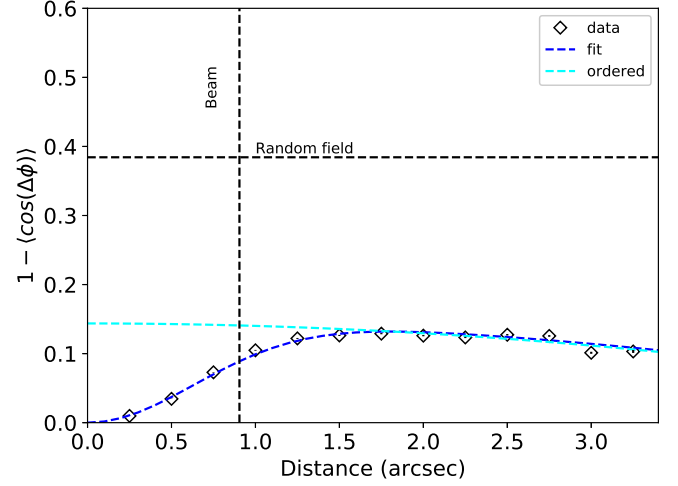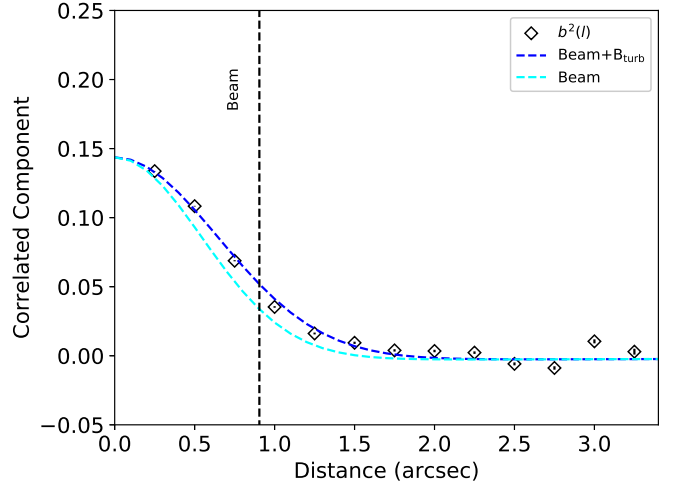
**Figure 9.** Same as Figure 8 but for MM4-Core4.

MM1, the well-aligned magnetic field and local gravity in the northeastern region suggests that the magnetic field morphology is shaped by gravity in this region, while the magnetic field and the local gravity in the southwestern region are poorly aligned, suggesting that the magnetic field has kept its own dynamics.

If the hydrostatic gas pressure is neglectable, the local ratio between magnetic field force $F_{\rm B}$ and the gravity force $F_{\rm G}$ can be measured by the magnetic field-to-gravity force ratio (Koch et al. 2012)

$$\Sigma_{\rm B} = \frac{\sin\psi}{\sin(90° - \delta)} = \frac{F_{\rm B}}{|F_{\rm G}|}. \qquad (21)$$

Figure 14 shows the $\Sigma_{\rm B}$ maps for MM1 and MM4. The median values of $\Sigma_{\rm B}$ in MM1 and MM4 are 0.47 and
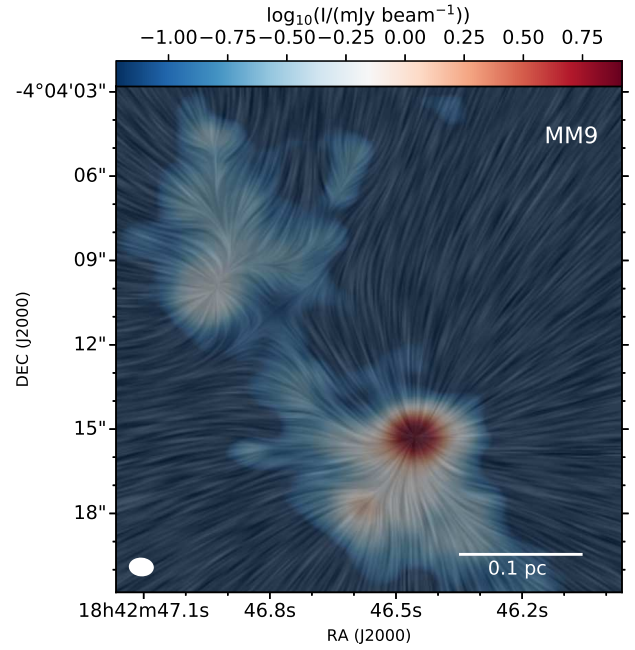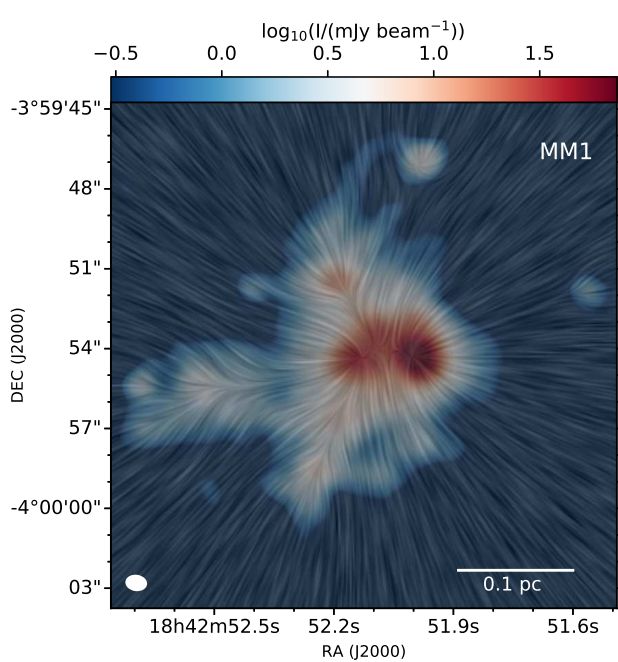
Figure 10. (Continued)
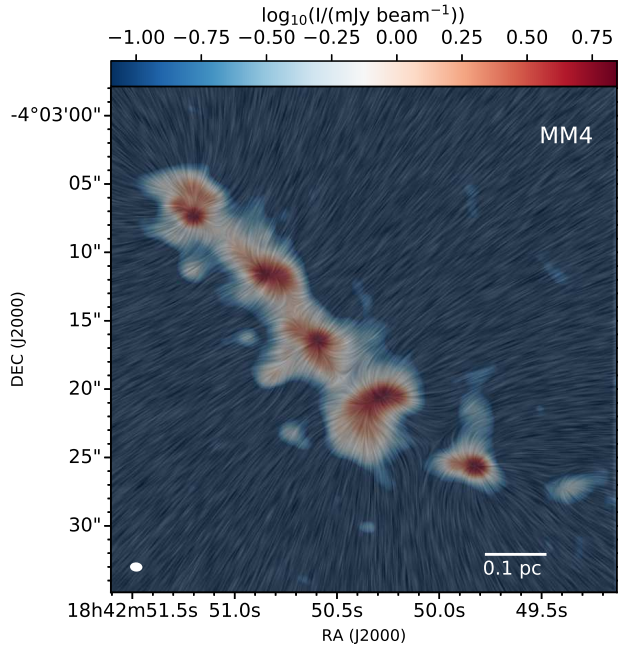
Figure 10. Local gravity orientation maps. The Stokes I of the ALMA 1.3 mm continuum is shown in color scales. The overlaid patterns are produced with the line integral convolution method (LIC, Cabral & Leedom 1993) and indicate the orientation of the local gravity ($\theta_{\rm LG}$).

0.27 respectively. The small values of $\Sigma_{\rm B}$ indicate that overall the magnetic field cannot solely balance the gravitational force.

4. DISCUSSION

4.1. *Uncertainty of the DCF method for super-Alfvénic cases*

The accuracy of the DCF method has been under investigation in the literature. The reliability of the DCF method can be tested with with numerical simulations (Ostriker et al. 2001; Padoan et al. 2001; Heitsch et al. 2001; Falceta-Gonçalves et al. 2008). Specifically, Heitsch et al. (2001) and Falceta-Gonçalves et al. (2008) investigated the effect of large angular dispersion and the effect of energy equipartition between the turbulent magnetic energy and the turbulent kinetic energy. Their results showed that the DCF method could overestimate the magnetic field strength for super-Alfvénic models.

The equipartition between the turbulent magnetic energy and the turbulent kinetic energy is a basic assumption of the DCF method. However, since the perturbation on the magnetic field cannot follow the strong kinetic motions for super-Alfvénic cases, the energy equipartition would be broken and the magnetic field strength would be overestimated (Heitsch et al. 2001; Falceta-Gonçalves et al. 2008).

Another basic assumption of the DCF method is that the dispersion of polarization position angles corresponds to the ratio between the turbulent and ordered
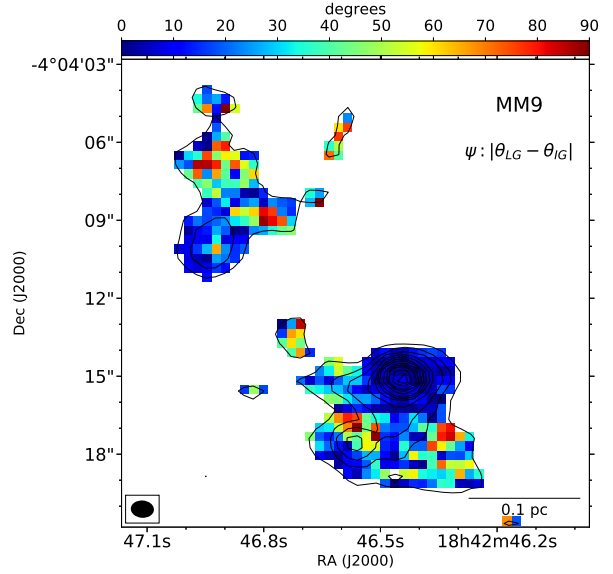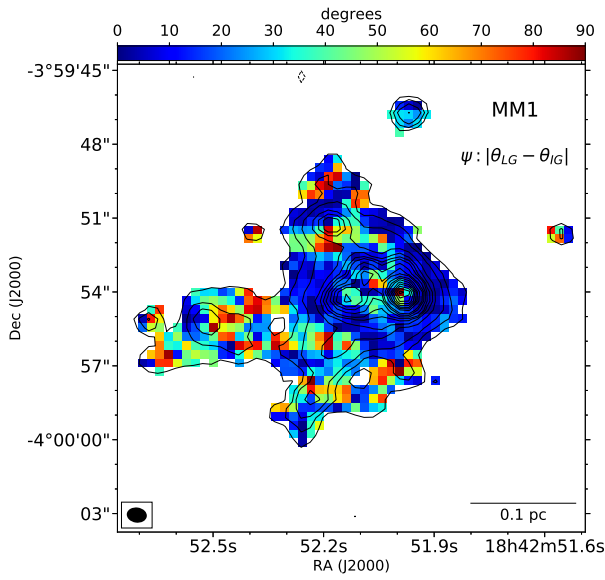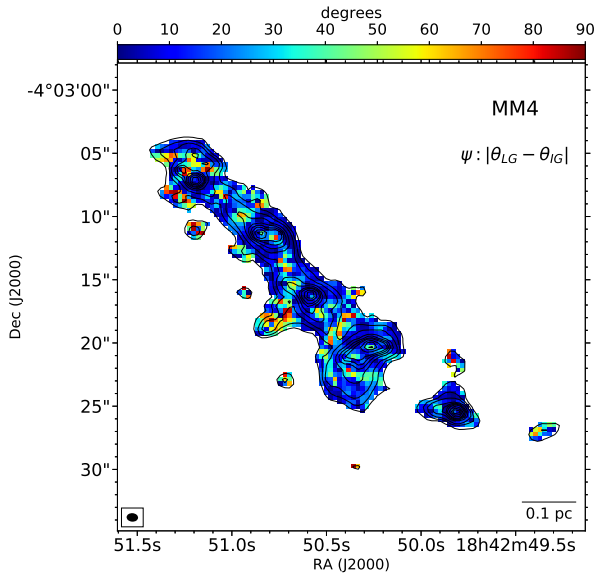
Figure 11. (Continued)

Figure 11. Angle difference between orientations of the intensity gradient and the local gravity ($\psi = |\theta_{\mathrm{IG}} - \theta_{\mathrm{LG}}|$). Contour levels are the same as those in Figure 2.

components of the magnetic field. For weak fields with Alfvén Mach number >1, the magnetic field lines can be easily distorted and the angular dispersion can approach that expected for a random field. As a consequence, the measured angular dispersion cannot reflect the true extent of the perturbed magnetic field and the magnetic field strength would be overestimated (Heitsch et al. 2001; Falceta-Gonçalves et al. 2008).

The magnetic field strength of MM1-Core1 and MM4-Core4 is derived from the ADF method (see Section 3.5). The ADF method improves the original DCF method by taking into account the signal-integration effect and the large-scale field. However, the ADF method does not correct for the aforementioned effects of energy equipartition and large angular dispersion. Since the two cores are in super-Alfvénic states (see Section 3.5), it is possible that the ADF method has overestimated the magnetic field strength in the two cores.

4.2. Dynamical state

The star formation process are governed by the complex interplay of self-gravity and competing processes (e.g., turbulence, thermal pressure, magnetic fields, stellar feedback, and rotation). For decades, the virial theorem has been used to study whether star-forming regions are stable against gravitational collapse. We briefly review the concept of the virial theorem and point out possible mistakes in some previous virial studies in Appendix A. Here we calculate the relevant parameters in MM1-Core1 and MM4-Core4, and discuss the implication on massive star formation.

4.2.1. Dynamic states in MM1-Core1 and MM4-Core4

We computed the virial masses and virial parameters for the two massive dense cores MM1-Core1 and MM4-Core4. The thermal velocity dispersion (1D sound speed, σ_{th}) is derived by

$$\sigma_{\mathrm{th}} = \sqrt{\frac{k_{\mathrm{B}}T}{\mu_{\mathrm{p}}m_{\mathrm{H}}}}, \tag{22}$$
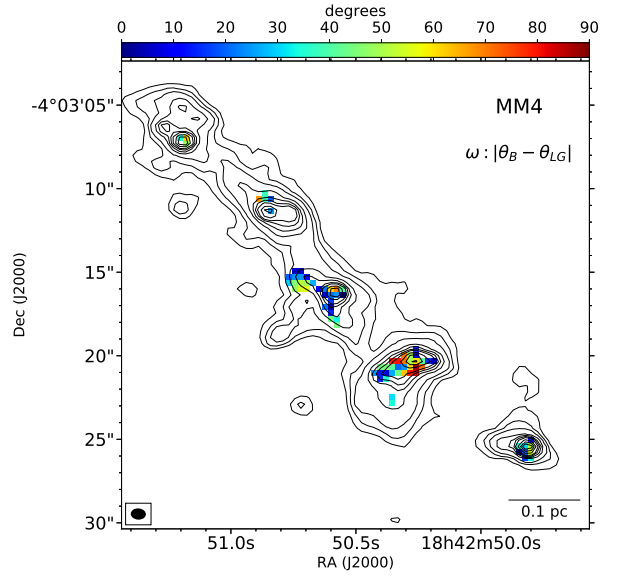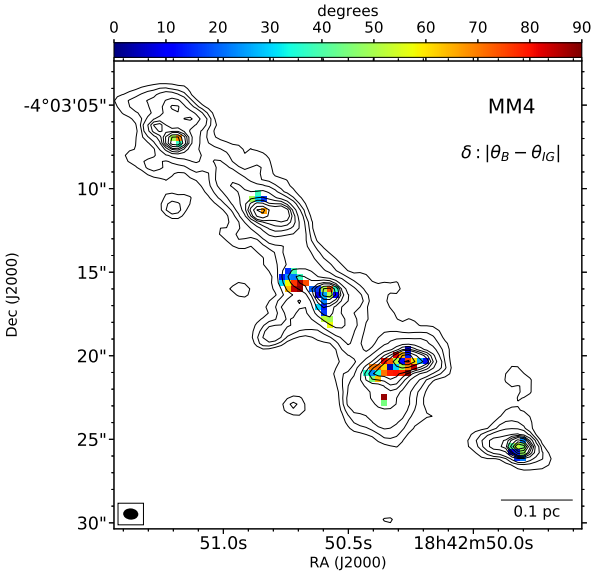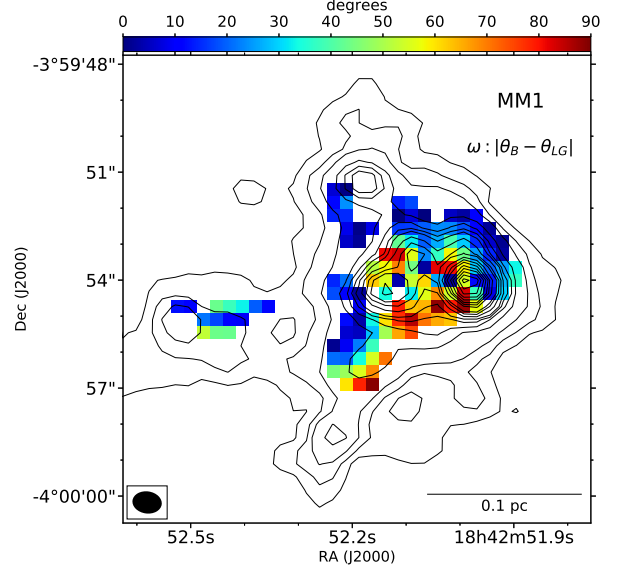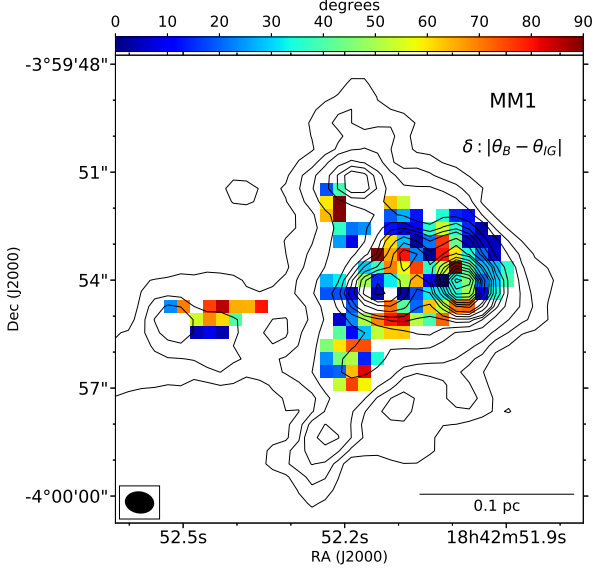
Figure 12. Angle difference between orientations of the magnetic field and the intensity gradient ($\delta = |\theta_{\mathrm{B}} - \theta_{\mathrm{IG}}|$). Values of δ are computed at where $PI/\sigma_{PI} > 3$. Contour levels are the same as those in Figure 2.

Figure 13. Angle difference between orientations of the magnetic field and the local gravity ($\omega = |\theta_{\mathrm{B}} - \theta_{\mathrm{LG}}|$). Values of ω are computed at where $PI/\sigma_{PI} > 3$. Contour levels are the same as those in Figure 2.

where $\mu_{\mathrm{p}} = 2.33$ is the conventional mean molecular weight per free particle. The 3D sound speed is estimated as $\sigma_{\mathrm{th,3D}} = \sqrt{3}\sigma_{\mathrm{th}}$. We adopted radial density profiles $\rho \propto r^{-a}$ ($a = 1.6$ and $a = 2.1$ for MM1-Core1 and MM4-Core4, respectively, Zhang et al. 2009) for the two cores. The kinetic virial mass is derived by

$$M_{\mathrm{k}} = \frac{3(5 - 2a)\sigma_{tot}^2 R}{(3 - a)G}, \qquad (23)$$

where $\sigma_{\mathrm{tot}} = \sqrt{\sigma_{\mathrm{th}}^2 + \sigma_{\mathrm{turb}}^2}$ is the total 1D gas velocity dispersion, $R = \mathrm{FWHM}_{\mathrm{mean}}$ is the radius of the core, and G is the gravitational constant. Similarly, the thermal virial mass M_{th} and the turbulent virial mass M_{turb} can be derived by replacing σ_{tot} with σ_{th} or σ_{turb}, respectively. The ordered magnetic virial mass is given by

(a)

(b)
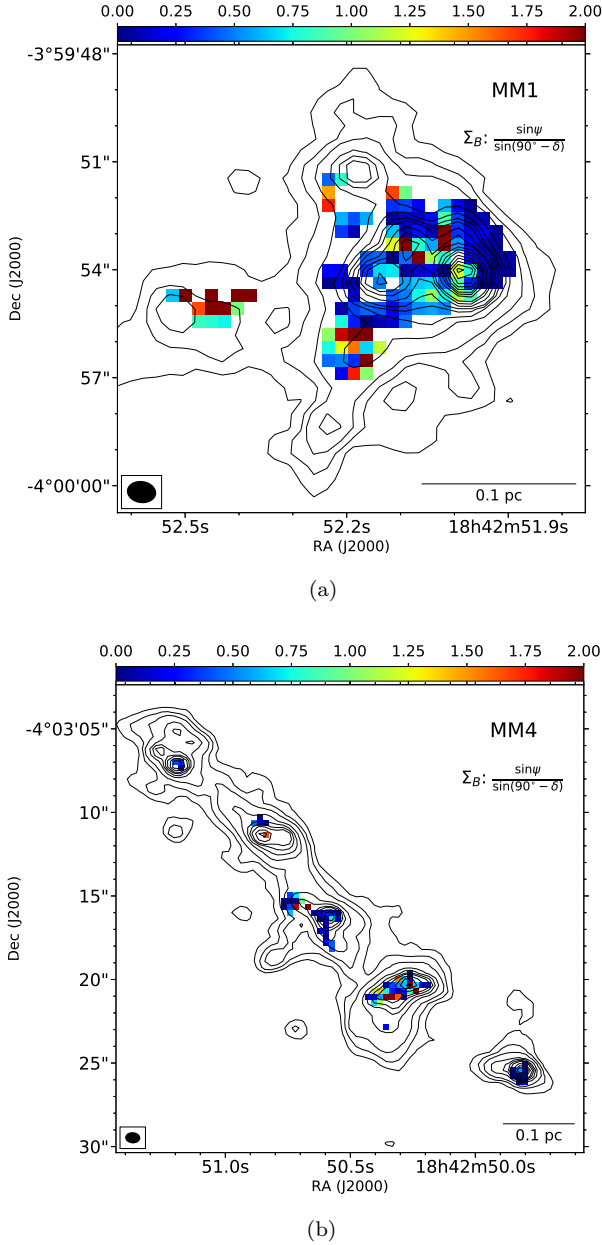
Figure 14. Maps of Σ_B. Values of Σ_B are computed at where $PI/\sigma_{PI} > 3$. Contour levels are the same as those in Figure 2.

$$M_B = \frac{\pi R^2 B}{\sqrt{\frac{3(3-a)}{2(5-2a)}\mu_0 \pi G}}, \tag{24}$$

in SI units or CGS units. The total virial mass accounting for both the ordered magnetic field and the kinetic motions is given by

$$M_{k+B} = \sqrt{M_B^2 + (\frac{M_k}{2})^2} + \frac{M_k}{2}. \tag{25}$$

The corresponding total virial parameter is

$$\alpha_{k+B} = \frac{M_{k+B}}{M}. \tag{26}$$

As indicated in Table 4, the turbulent magnetic energy is comparable to the ordered magnetic energy. If we take into account the turbulent magnetic energy in the virial analysis, the modified magnetic virial mass M_B^{mod}, total virial mass M_{k+B}^{mod}, and total virial parameter α_{k+B}^{mod} could be derived from Equations 24, 25, and 26 by replacing B with $B(1 + B_t^2/B_0^2)^{\frac{1}{2}}$.

Table 5 lists the calculated parameters of the two cores. The nonthermal kinetic energy, thermal kinetic energy, and ordered magnetic energy can be compared by the square of the 3D turbulent velocity dispersion ($\sigma_{turb,3D}$), 3D thermal velocity dispersion ($\sigma_{turb,3D}$), and 3D Alfvén velocity ($V_{A,3D}$). Both cores have $(\sigma_{turb,3D})^2 \gg (\sigma_{th,3D})^2$ (super-sonic) and $(V_{A,3D})^2 \gg (\sigma_{th,3D})^2$, which means the thermal energy only plays a neglectable role in the energy balance. The two cores also have $(\sigma_{turb,3D})^2 > (V_{A,3D})^2$, suggesting that the turbulent energy exceeds the ordered magnetic energy. **The two cores have $(\sigma_{turb,3D})^2 \sim (V_{A,3D}^{mod})^2$, which means the total magnetic energy is comparable to the turbulent energy.** Another way to assess the role of the three forces is to compare the maximum mass that can be supported by each force. The mass ratios show similar trends to the energy ratios in the two cores, except that the ordered magnetic virial mass is larger than the turbulent virial mass in MM4-Core4, which is in contrast to the energy ratio in this core ($E_{turb} > E_B$).

The modified total virial parameters α_{k+B}^{mod} in MM1-Core1 and MM4-Core4 are found to be less than 1 (i.e., sub-virial). As shown in many previous studies, the main uncertainty comes from the mass estimation. If the mass is overestimated by a factor of 2 (i.e., the magnetic field strength overestimated by a factor of $\sqrt{2}$, if we ignore other sources of uncertainties), the α_{k+B}^{mod} of MM1-Core1 and MM4-Core4 would be 1.3 and 0.58, respectively. Since the α_{k+B}^{mod} in MM4-Core4 is much less than 1, it is very unlikely that MM4-Core4 is in virial equilibrium even with consideration of the large uncertainty of the analysis. However, we cannot rule out the possibility that MM1-Core1 is in virial equilibrium. More accurate estimations of the dust opacity might be required to reduce the uncertainty of the estimated virial parameter of MM1-Core1. Due to the limited angular resolution of our polarization observations and the lack of observations of appropriate turbulence tracers, we refrain from discussing the virial parameters at condensation scale.

4.2.2. *Non-equilibrium massive star formation*

Table 5. Physical parameters relevant to the virial analysis

Source	$\sigma_{\mathrm{th,3D}}$	$\sigma_{\mathrm{turb,3D}}$	$V_{\mathrm{A,3D}}$	$V_{\mathrm{A,3D}}^{\mathrm{mod}}$ a	M	M_{th}	M_{turb}	M_{B}	$M_{\mathrm{B}}^{\mathrm{mod}}$	$M_{\mathrm{k+B}}$	$M_{\mathrm{k+B}}^{\mathrm{mod}}$	$\alpha_{\mathrm{k+B}}$	$\alpha_{\mathrm{k+B}}^{\mathrm{mod}}$
	(km s^{-1})	(km s^{-1})	(km s^{-1})	(km s^{-1})	$M_\odot$	$M_\odot$	($M_\odot$)	($M_\odot$)	($M_\odot$)	($M_\odot$)	($M_\odot$)		
MM1-Core1	0.33	2.42	1.5	2.2	212.4	1.9	102.8	61.1	95.5	132.8	161.2	0.63	0.76
MM4-Core4	0.24	0.80	0.51	0.75	42.6	0.58	6.6	7.3	11.4	11.8	15.6	0.28	0.37

a**Equivalent 3D total Alfvén velocity** $V_{\mathrm{A,3D}}^{\mathrm{mod}} = \frac{B(1+B_{\mathrm{t}}^2/B_0^2)^{\frac{1}{2}}}{\sqrt{\mu_0\rho}}$ **taking into account both the ordered magnetic field and the turbulent magnetic field.**

Previous observations show that a significant amount of massive star forming clumps and cores are in sub-virial states (Pillai et al. 2011; Kauffmann et al. 2013; Tan et al. 2013; Liu et al. 2015; Zhang et al. 2015; Ohashi et al. 2016; Sanhueza et al. 2017; Lu et al. 2018). However, there are no direct measurements of the magnetic field strength in their analyses, while the magnetic field could provide significant support to regulate the high-mass star formation (Frau et al. 2014; Pillai et al. 2015).

Our observations and calculations offer direct evidence of the role of magnetic fields in the dynamical state of two massive dense cores. As discussed in Section 4.2.1, MM4-Core4 is in a sub-virial state and MM1-Core1 is likely in a sub-virial state. The sub-virial state indicates that massive dense cores could undergo dynamical collapse in non-equilibrium in the early stage of star formation, which is in agreement with the competitive accretion model. Considering that MM1-Core1 is in a later evolution stage than MM4-Core4 (Zhang et al. 2009), the higher virial parameter of MM1-Core1 might suggest enhanced supports from the gas motion and the magnetic field as cores evolve.

4.3. Comparing outflow axis with magnetic field orientation in condensation

The importance of magnetic fields in star formation can be studied by comparing the orientations of molecular outflows and ambient magnetic fields. Results from MHD simulations (Lee et al. 2017) suggest that strong ambient magnetic fields tend to align the axis of protostellar outflows because of magnetic braking (Allen et al. 2003), while the outflow-field orientation in the weak-field case is more random.

Observationally, a compilation of all of the outflow-versus-magnetic-field angles derivable to date in low-mass protostellar cores shows that overall the magnetic fields in low-mass dense cores are randomly aligned with outflows (Hull, & Zhang 2019). Galametz et al. (2018) found a bimodal distribution of the angles between the envelope-scale magnetic field orientation and outflow axis in low-mass class 0 objects, suggesting that the

magnetic field could play an important role in regulating the direction of outflows in the early stage of low-mass star formation.

In the case of massive star formation region, an SMA survey toward high-mass clumps found no strong correlation between the outflow axis and the magnetic field orientation in evolved dense cores with a total of 21 outflow samples (Zhang et al. 2014). Since molecular outflows are believed to be driven by MHD winds originated in or near the circumstellar disk (Shu et al. 2000; Pudritz et al. 2006), the observed misalignment between the magnetic field orientation and the outflow axis indicates a less dynamically important role of magnetic fields from the core scale down to the disk scale.

With ALMA CO (2-1) and SiO (5-4) observations, Kong et al. (2019b) has determined the plane-of-sky position angle of the outflows ($\theta_{\mathrm{outflow}}$) in IRDC G28.34 (except those in MM1). Our polarization observations have resolved the magnetic field structure down to scales of ∼0.02 pc, which allows us to compare the outflow axis with the magnetic field orientation at condensation scales. Since MM1 is in a later stage of star formation and the position angle of the outflows in MM1 is not determined due to the complexity of the CO emission, we limit the comparison in MM4 and MM9.

The magnetic field orientation in each condensation (θ_{B}) in MM4 and MM9 is measured within one ALMA synthesized beam. There are 15 outflows in MM4 and MM9, among which 12 of them are associated with polarization detections in the condensation (see Figure 15). Figure 16 shows the angular difference between the outflow axis and the magnetic field orientation in the condensations where outflows originate for the 12 outflow samples in MM4 and MM9. The angular difference between the outflow axis and the field orientation appears to be in an approximate bimodal distribution, where the outflow axis tends to be either parallel or perpendicular to the orientation of magnetic fields. In half of the objects, the magnetic field is aligned within 10° of the outflow axis, suggesting that magnetic fields could be

dynamically important from the condensation scale to the disk scale in the early stage of high-mass star formation. However, the observed magnetic field and outflow position angles are projected on the plane of sky. Observations toward larger samples of magnetic fields in IRDCs are essential to help us to rule out the possibility that the observed distribution is due to the projection effect.

4.4. Fragmentation and clustered star formation in MM1

The two competing massive star formation models have different predictions on the fragmentaion of molecular clouds. The competitive accretion model proposes that the initial fragments in molecular clouds should be in thermal Jeans mass. The fragments and protostars therein near the gravitational center can thus accrete at a higher rate and form massive stars. Alternatively, the turbulent core accretion model suggests massive stars are formed via the monolithic collapse of a massive core that is supported by turbulent pressure rather than thermal pressure.

Our observations may help to distinguish between the two models. To quantify the separation of condensations in MM1, we applied the minimum spanning tree (hereafter MST) technique on these condensations using the python package MiSTree (Naidoo 2019). The MST method connects the condensations with straight lines and minimizes the sum of the line length. Figure 17 show the MST for MM1. The separation of condensations in MM1 ranges from 0.025 pc to 0.16 pc.

Since the maximum recoverable scale of our ALMA observations is $\sim 7''$ for MM1, we focus on interpreting the fragmentation in the core MM1-Core1 (including Condensations 1, 2, 3, 4, 5, and 6) that has a size of $\sim 6''$. The separation of condensations in MM1-Core1 ranges from 0.025 pc to 0.058 pc and the average separation ($L_{av,MST}$) of these condensations is calculated to be 0.044 pc. As the measured separations are projected on the plane-of-sky, we multiplied the observed separation by a factor of $\pi/2$ to correct for the statistical projection effect (Sanhueza et al. 2019) and the corrected average separation ($L_{av,MST,cor}$) is estimated to be 0.069 pc. The mass of the condensations in MM1-Core1 ranges from 3.7 to 35.5 M$_\odot$ (see Table 3) and the average mass (M_{av}) of these condensations is calculated to be 14.3 M$_\odot$.

With a temperature of 30 K and a density of 3.2×10^6 cm^{-3}, the thermal Jeans length

$$\lambda_{\mathrm{J,th}} = \sigma_{\mathrm{th,3D}} \sqrt{\frac{\pi}{G\mu_{\mathrm{H_2}} m_{\mathrm{H}} n_{\mathrm{H_2}}}} \qquad (27)$$

and the thermal Jeans mass

$$M_{\mathrm{J,th}} = \frac{4}{3}\pi \mu_{\mathrm{H_2}} m_{\mathrm{H}} n_{\mathrm{H_2}} \left(\frac{\lambda_{\mathrm{J,th}}}{2}\right)^3 \qquad (28)$$

of MM1-Core1 are estimated to be 0.019 pc and 0.76 M$_\odot$, respectively. The M_{av} is about 19 times larger than the $M_{\mathrm{J,th}}$ and the $L_{av,MST,cor}$ is about 3 times larger than the $\lambda_{\mathrm{J,th}}$. Considering that the resolution of our observations ($\sim$0.02 pc) is insufficient to resolve the foreshortened thermal Jeans length ($2/\pi$ times $\lambda_{\mathrm{J,th}}$) of 0.012 pc, we can not rule out the possibility that the detected condensations would further fragment into smaller structures with separations $\sim \lambda_{\mathrm{J,th}}$. However, even if each condensation in MM1-Core1 further fragments into several smaller structures, the average mass of the fragments is unlikely to be close to the $M_{\mathrm{J,th}}$ since M_{av} is much larger than $M_{\mathrm{J,th}}$.

Replacing the thermal velocity dispersion with the turbulent velocity dispersion in Equations 27 and 28, the turbulent Jeans length and the turbulent Jeans mass in MM1-Core1 are estimated to be 0.14 pc and 309 M$_\odot$, respectively, which are much larger than the $L_{av,MST,cor}$ and the M_{av}.

Thus, we conclude that the fragmentation in MM1-Core1 cannot be solely explained by the thermal Jeans fragmentation nor the turbulent Jeans fragmentation, which are inconsistent with either the competitive accretion model or the turbulent core accretion model. These discrepancies indicate that the physical condition in MM1-Core1 might have deviated from the initial condition of the core that controls the fragmentation process. On the other hand, we find that the mass of the condensations near the core center is more massive than that of the condensations in the outer region (see Table 3). Thus, we expect MM1 to form a cluster of stars with several massive stars near the center and a population of low-mass stars in the outer region. This picture seems to agree with the competitive accretion model.

5. SUMMARY

With ALMA 1.3 mm dust polarization observations, we have presented a study of the magnetic field of three massive clumps in the IRDC G28.34. The main conclusions are as follows:

1. Polarized dust emission are detected in all the three clumps. The magnetic field morphology varies in different regions. Trends of decreasing polarization percentage with increasing intensity are detected in MM1 and MM4. The P-I relation in MM1 is shallower than that in MM4, which might be explained by the improved grain alignment efficiency due to enhanced internal radiation in more evolved regions.
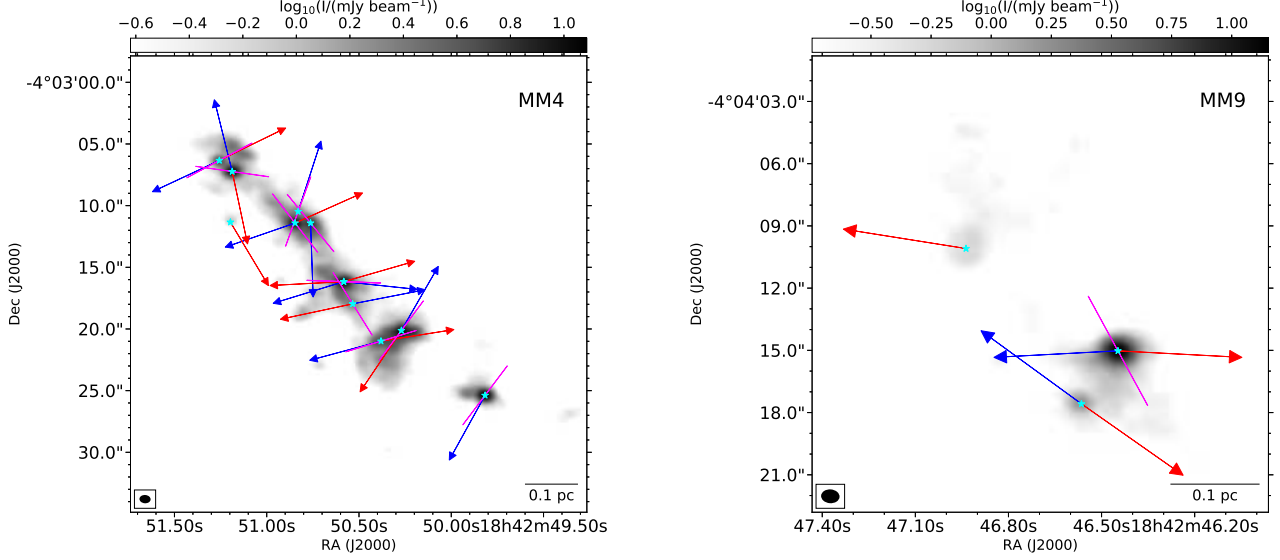
Figure 15. Summary of orientations of magnetic fields and outflows in MM4 and MM9. The Stokes I of the 1.3 mm continuum is shown in grey scale. The star symbols denote the position of dense condensations (Zhang et al. 2015; Kong 2019a) that are associated with outflows. The large magenta bars indicate the average magnetic orientation for each condensation. The blue- and red-shifted outflow lobes are shown as blue and red dashed arrows, respectively. Bars and arrows are of arbitrary unit length.
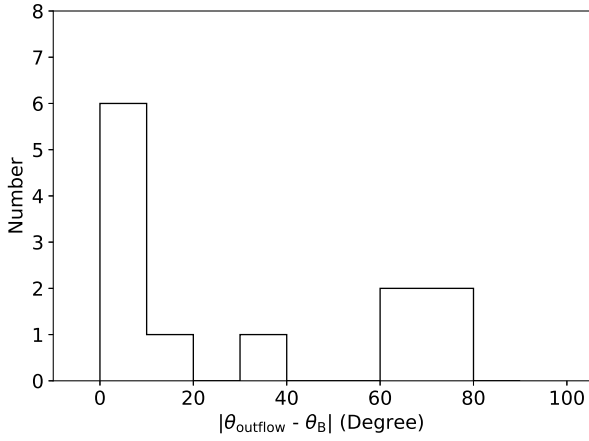
Figure 16. Angular difference between the outflow axis and the ∼0.02 pc scale magnetic field orientation in the condensations where outflows originate for the 12 outflow samples in MM4 and MM9.

2. From the dust polarization maps, we measured the plane-of-sky magnetic field strength in two massive dense cores, MM1-Core1 ($M = 212.4 M_\odot$) and MM4-Core4 ($M = 43.0 M_\odot$), with the autocorrelation function method. The $B_{\rm pos}$ is found to be ∼1.6 mG and ∼0.32 mG in MM1-Core1 and MM4-Core4, respectively.
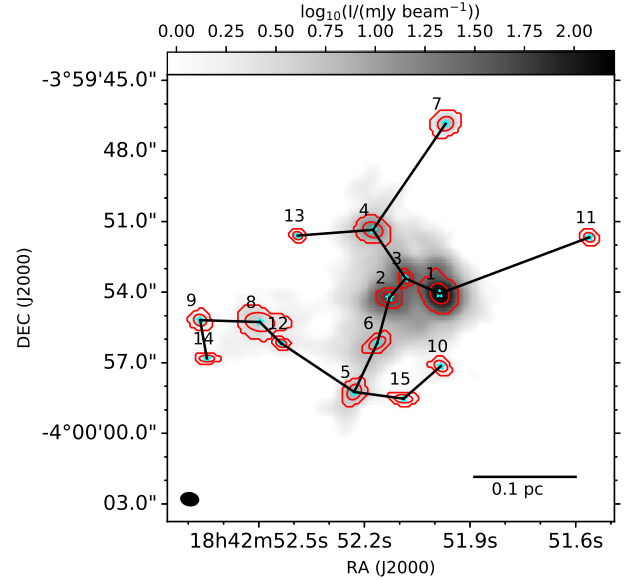
Figure 17. Results of the MST (shown in black segments) in MM1. Red contours and ellipses are the same as those in Figure 3. Star symbols mark the position of the condensations identified by dendrogram.

3. We studied the dynamical state in MM1-Core1 and MM4-Core4 by calculating the virial parameter that includes both the turbulence and the magnetic field. **In both cores, the ordered magnetic energy is smaller than the turbu-**

lent energy and the total magnetic energy is comparable to the turbulent energy. The results of the virial analysis suggest that MM4-Core4 is in a sub-virial state and MM1-Core1 is likely in a sub-virial state, which signifies a dynamical massive star formation in non-equilibrium.

4. We compared the orientations of the magnetic field, local gravity, and intensity gradient with the polarization-intensity gradient-local gravity method. We found that the intensity gradient closely follows the local gravity in the three clumps. The magnetic field is found to be randomly aligned with the intensity gradient, but better aligned with the local gravity in MM1 and MM4. The average magnetic field to gravity force ratio are found to be smaller than 1 in MM1 and MM4, which suggests that the magnetic force cannot solely prevent the gravitational collapse.

5. With a total of 12 outflow samples in MM4 and MM9, the angle between orientations of the magnetic field at condensation scales and the outflow axis shows an approximate bimodal distribution with half of the outflows aligned within 10° of the magnetic field, which suggests that magnetic fields could play an important role from the condensation scale to the disk scale in the early stage of massive star formation.

6. We identified the dense condensations in MM1 with the dendrogram method and characterized the separation of these condensations using the minimum spanning tree technique. The mass of the condensations and the average minimum separation between condensations in MM1-Core1 are found to be larger than the values predicted by thermal Jeans fragmentation and smaller than the values predicted by turbulent Jeans fragmentation. Thus we propose that the physical condition in MM1-Core1 might has deviated from the initial condition that controls the fragmentation.

REFERENCES

Andersson, B.-G., Lazarian, A., & Vaillancourt, J. E. 2015, ARA&A, 53, 501

Astropy Collaboration, Robitaille, T. P., Tollerud, E. J., et al. 2013, A&A, 558, A33

Allen, A., Li, Z.-Y., & Shu, F. H. 2003, ApJ, 599, 363

Beckwith, S. V. W., & Sargent, A. I. 1991, ApJ, 381, 250

Bertoldi, F., & McKee, C. F. 1992, ApJ, 395, 140

Beuther, H., Soler, J. D., Vlemmings, W., et al. 2018, A&A, 614, A64

Beuther, H., Leurini, S., Schilke, P., et al. 2007, A&A, 466, 1065

Bonnell, I. A., Bate, M. R., Clarke, C. J., et al. 1997, MNRAS, 285, 201

Bonnor, W. B. 1956, MNRAS, 116, 351

Butler, M. J., & Tan, J. C. 2009, ApJ, 696, 484

Cabral, B., & Leedom, L. C. 1993, in Special Interest Group on GRAPHics and Interactive Techniques Proceedings, 263

Cao, Y., Qiu, K., Zhang, Q., et al. 2019, ApJS, 241, 1

Carey, S. J., Clark, F. O., Egan, M. P., et al. 1998, ApJ, 508, 721

Chandrasekhar, S., & Fermi, E. 1953, ApJ, 118, 113

Chen, H.-R., Liu, S.-Y., Su, Y.-N., et al. 2010, ApJL, 713, L50

Chen, H.-R., Su, Y.-N., Liu, S.-Y., et al. 2007, ApJL, 654, L87

Cheng, Y., Tan, J. C., Liu, M., et al. 2018, ApJ, 853, 160

Crutcher, R. M., Nutter, D. J., Ward-Thompson, D., et al. 2004, ApJ, 600, 279

Davis, L. 1951, Physical Review, 81, 890

Ebert, R. 1957, ZA, 42, 263

Falceta-Gonçalves, D., Lazarian, A., & Kowal, G. 2008, ApJ, 679, 537

Feng, S., Caselli, P., Wang, K., et al. 2019, ApJ, 883, 202

Feng, S., Beuther, H., Zhang, Q., et al. 2016, ApJ, 828, 100

Feng, S., Beuther, H., Zhang, Q., et al. 2016, A&A, 592, A21

Frau, P., Girart, J. M., Zhang, Q., et al. 2014, A&A, 567, A116

Galametz, M., Maury, A., Girart, J. M., et al. 2018, A&A, 616, A139

Girart, J. M., Frau, P., Zhang, Q., et al. 2013, ApJ, 772, 69

Girart, J. M., Beltrán, M. T., Zhang, Q., et al. 2009, Science, 324, 1408

Heitsch, F., Zweibel, E. G., Mac Low, M.-M., et al. 2001, ApJ, 561, 800

Hennebelle, P., & Chabrier, G. 2008, ApJ, 684, 395

Henning, T., Michel, B., & Stognienko, R. 1995, Planet. Space Sci., 43, 1333

Hildebrand, R. H., Kirby, L., Dotson, J. L., Houde, M., & Vaillancourt, J. E. 2009, ApJ, 696, 567

Hildebrand, R. H. 1983, QJRAS, 24, 267

Ho, P. T. P., & Townes, C. H. 1983, ARA&A, 21, 239

Houde, M., Hull, C. L. H., Plambeck, R. L., et al. 2016, ApJ, 820, 38

Houde, M., Vaillancourt, J. E., Hildebrand, R. H., Chitsazzadeh, S., & Kirby, L. 2009, ApJ, 706, 1504

Hull, C. L. H., & Zhang, Q. 2019, Frontiers in Astronomy and Space Sciences, 6, 3

Hunter, J. D. 2007, Computing in Science and Engineering, 9, 90

Juvela, M., Guillet, V., Liu, T., et al. 2018, A&A, 620, A26

Kataoka, A., Muto, T., Momose, M., et al. 2015, ApJ, 809, 78

Kauffmann, J., Pillai, T., & Goldsmith, P. F. 2013, ApJ, 779, 185

Kirk, J. M., Ward-Thompson, D., Palmeirim, P., et al. 2013, MNRAS, 432, 1424

Koch, P. M., Tang, Y.-W., & Ho, P. T. P. 2012, ApJ, 747, 79

Kong, S., Arce, H. G., Maureira, M. J., et al. 2019, ApJ, 874, 104

Kong, S. 2019, ApJ, 873, 31

Kong, S., Tan, J. C., Caselli, P., et al. 2018, ApJ, 867, 94

Kong, S., Tan, J. C., Arce, H. G., et al. 2018, ApJL, 855, L25

Krumholz, M. R. 2014, PhR, 539, 49

Krumholz, M. R., McKee, C. F., & Klein, R. I. 2005, Nature, 438, 332

Kwon, J., Doi, Y., Tamura, M., et al. 2018, ApJ, 859, 4

Lazarian, A. 2007, JQSRT, 106, 225

Lazarian, A., & Hoang, T. 2007, MNRAS, 378, 910

Lee, J. W. Y., Hull, C. L. H., & Offner, S. S. R. 2017, ApJ, 834, 201

Lin, Y., Liu, H. B., Dale, J. E., et al. 2017, ApJ, 840, 22

Liu, J., Qiu, K., Berry, D., et al. 2019, ApJ, 877, 43

Liu, M., Tan, J. C., Cheng, Y., et al. 2018, ApJ, 862, 105

Liu, T., Li, P. S., Juvela, M., et al. 2018, ApJ, 859, 151

Liu, H. B., Galván-Madrid, R., Jiménez-Serra, I., et al. 2015, ApJ, 804, 37

Lu, X., Zhang, Q., Liu, H. B., et al. 2018, ApJ, 855, 9

McKee, C. F., & Tan, J. C. 2002, Nature, 416, 59

McMullin, J. P., Waters, B., Schiebel, D., et al. 2007, Astronomical Data Analysis Software and Systems XVI, 127

Motte, F., Bontemps, S., Schilke, P., et al. 2007, A&A, 476, 1243

Motte, F., & André, P. 2001, A&A, 365, 440

Naghizadeh-Khouei, J., & Clarke, D. 1993, A&A, 274, 968

Nakano, T., & Nakamura, T. 1978, PASJ, 30, 671

Naidoo, K. 2019, The Journal of Open Source Software, 4, 1721

Ohashi, S., Sanhueza, P., Chen, H.-R. V., et al. 2016, ApJ, 833, 209

Ostriker, E. C., Stone, J. M., & Gammie, C. F. 2001, ApJ, 546, 980

Padoan, P., Goodman, A., Draine, B. T., et al. 2001, ApJ, 559, 1005

Pattle, K., & Fissel, L. 2019, Frontiers in Astronomy and Space Sciences, 6, 15

Pattle, K., Lai, S.-P., Hasegawa, T., et al. 2019, ApJ, 880, 27

Pattle, K., Ward-Thompson, D., Berry, D., et al. 2017, ApJ, 846, 122

Pattle, K., Ward-Thompson, D., Kirk, J. M., et al. 2015, MNRAS, 450, 1094

Pillai, T., Kauffmann, J., Tan, J. C., et al. 2015, ApJ, 799, 74

Pillai, T., Kauffmann, J., Wyrowski, F., et al. 2011, A&A, 530, A118

Pillai, T., Wyrowski, F., Carey, S. J., et al. 2006, A&A, 450, 569

Perault, M., Omont, A., Simon, G., et al. 1996, A&A, 315, L165

Pudritz, R. E., Rogers, C. S., & Ouyed, R. 2006, MNRAS, 365, 1131

Qiu, K., Zhang, Q., Menten, K. M., et al. 2014, ApJL, 794, L18

Rathborne, J. M., Jackson, J. M., & Simon, R. 2006, ApJ, 641, 389

Ragan, S., Henning, T., Krause, O., et al. 2012, A&A, 547, A49

Rao, R., Crutcher, R. M., Plambeck, R. L., et al. 1998, ApJL, 502, L75

Robitaille, T., & Bressert, E. 2012, APLpy: Astronomical Plotting Library in Python, Astrophysics Source Code Library, ascl:1208.017

Rosolowsky, E. W., Pineda, J. E., Kauffmann, J., et al. 2008, ApJ, 679, 1338

Roy, A., André, P., Palmeirim, P., et al. 2014, A&A, 562, A138

Sanhueza, P., Contreras, Y., Wu, B., et al. 2019, ApJ, 886, 102

Sanhueza, P., Jackson, J. M., Zhang, Q., et al. 2017, ApJ, 841, 97

Shu, F. H., Najita, J. R., Shang, H., & Li, Z.-Y. 2000, in Protostars and Planets IV, ed. V. Manning, A. P. Boss, & S. S. Russell (Tucson, AZ: Univ. Arizona Press), 789

Shu, F. H., Adams, F. C., & Lizano, S. 1987, ARA&A, 25, 23

Simon, R., Rathborne, J. M., Shah, R. Y., et al. 2006, ApJ, 653, 1325

Soam, A., Liu, T., Andersson, B.-G., et al. 2019, ApJ, 883, 95

Soam, A., Pattle, K., Ward-Thompson, D., et al. 2018, ApJ, 861, 65

Tan, J. C., Kong, S., Zhang, Y., et al. 2016, ApJL, 821, L3

Tan, J. C., Beltrán, M. T., Caselli, P., et al. 2014, Protostars and Planets VI, 149

Tan, J. C., Kong, S., Butler, M. J., et al. 2013, ApJ, 779, 96

Tang, Y.-W., Koch, P. M., Peretto, N., et al. 2019, ApJ, 878, 10

Tang, Y.-W., Ho, P. T. P., Girart, J. M., et al. 2009, ApJ, 695, 1399

Tazaki, R., Lazarian, A., & Nomura, H. 2017, ApJ, 839, 56

Terebey, S., Chandler, C. J., & Andre, P. 1993, ApJ, 414, 759

Vaillancourt, J. E. 2006, PASP, 118, 1340

Wang, Ke . 2018, Research Notes of the American Astronomical Society, 2, 52

Wang, K., Zhang, Q., Wu, Y., et al. 2012, ApJL, 745, L30

Wang, K., Zhang, Q., Wu, Y., et al. 2011, ApJ, 735, 64

Wang, Y., Zhang, Q., Pillai, T., et al. 2008, ApJL, 672, L33

Wang, Y., Zhang, Q., Rathborne, J. M., et al. 2006, ApJL, 651, L125

Ward-Thompson, D., Pattle, K., Bastien, P., et al. 2017, ApJ, 842, 66

Yang, H., Li, Z.-Y., Looney, L., et al. 2016, MNRAS, 456, 2794

Zhang, Q., Wang, K., Lu, X., et al. 2015, ApJ, 804, 141

Zhang, Q., Qiu, K., Girart, J. M., et al. 2014, ApJ, 792, 116

Zhang, Q., Wang, Y., Pillai, T., et al. 2009, ApJ, 696, 268

APPENDIX

A. VIRIAL THEOREM

Ignoring the surface kinetic energy, the virial theorem is written as:

$$\frac{1}{2}\frac{d^2 I}{dt^2} = 2E_\mathrm{k} + E_\mathrm{B} + E_\mathrm{G}, \tag{A1}$$

where I is the moment of inertia, E_k is the kinetic energy, E_B is the magnetic energy, and E_G is the gravitational energy. For a sphere with a radial density profile $\rho \propto r^{-a}$ (for a uniform density, $a = 0$), the gravitational energy is given by

$$E_\mathrm{G} = -\frac{(3-a)}{(5-2a)}\frac{GM^2}{R}, \tag{A2}$$

where G is the gravitational constant, M is the mass of the considered structure, and R is the radius of the structure. The magnetic energy is given by

$$E_\mathrm{B} = \frac{B^2 V}{2\mu_0}, \tag{A3}$$

where $V = 4\pi R^3/3$ is the volume of the structure. The kinetic energy is the sum of the thermal energy (E_th) and the turbulent energy (E_turb):

$$E_\mathrm{k} = E_\mathrm{th} + E_\mathrm{turb} = \frac{3}{2}M\sigma_{tol}^2, \tag{A4}$$

where σ_tot is the total 1D gas velocity dispersion. The thermal energy and the turbulent energy can be derived by

$$E_\mathrm{th} = \frac{3}{2}M\sigma_\mathrm{th}^2, \tag{A5}$$

and

$$E_\mathrm{turb} = \frac{3}{2}M\sigma_\mathrm{turb}^2, \tag{A6}$$

respectively, where σ_th is the 1D thermal velocity dispersion and σ_turb is the 1D turbulent velocity dispersion.

For a non-magnetized ($E_\mathrm{B} = 0$) sphere, the structure is stable when $2E_\mathrm{k} + E_\mathrm{G} < 0$, which requires $M < M_\mathrm{k}$, where

$$M_\mathrm{k} = \frac{3(5-2a)\sigma_{tot}^2 R}{(3-a)G} \tag{A7}$$

is the kinetic virial mass. Similarly, we can define the thermal virial mass M_th and the turbulent virial mass M_turb by replacing σ_{tot} with the corresponding velocity dispersion to account for the thermal component and the turbulent component of the virial mass separately. Bertoldi, & McKee (1992) introduced a kinetic virial parameter

$$\alpha_k = \frac{2E_\mathrm{k}}{|E_\mathrm{G}|} = \frac{3(5-2a)\sigma_{tot}^2 R}{(3-a)GM} = \frac{M_\mathrm{k}}{M} \tag{A8}$$

to represent the ratio of the kinetic energy and the gravitational energy. We note that $M < M_\mathrm{k}$ (kinetically super-virial) is equivalent to $\alpha_k > 1$. For comparison with M_k, a Bonnor-Ebert sphere (Bonnor 1956; Ebert 1957) in isothermal hydrostatic equilibrium is stable when $M < M_\mathrm{BE}$, where M_BE is the Bonnor-Ebert critical mass given by

$$M_\mathrm{BE} = 2.43\frac{\sigma_{tot}^2 R}{G}. \tag{A9}$$

For a uniform sphere (a=0), $M < M_\mathrm{BE}$ is equivalent to $\alpha_k > 2.06$.

If the kinetic energy is neglectable ($E_\mathrm{k} = 0$), a stable sphere has $E_\mathrm{B} + E_\mathrm{G} < 0$, which implies $M < M_\mathrm{B}$, where

$$M_\mathrm{B} = \frac{\pi R^2 B}{\sqrt{\frac{3(3-a)}{2(5-2a)}\mu_0 \pi G}} \tag{A10}$$

is the magnetic virial mass in SI units or CGS units. We noticed some previous studies (e.g., Hennebelle, & Chabrier 2008; Pillai et al. 2011; Ohashi et al. 2016; Sanhueza et al. 2017; Hull, & Zhang 2019) have written the magnetic virial mass of a uniform ($a=0$) sphere as

$$M'_{\rm B} = \frac{5RV^2_{\rm A,3D}}{6G} = \frac{5RB^2}{6\mu_0\rho G} = \frac{10\pi R^4 B^2}{9\mu_0 GM},\qquad(A11)$$

where $V_{\rm A,3D} = \frac{B}{\sqrt{\mu_0\rho}}$ is the 3D Alfvén velocity in SI units or CGS units. The $M'_{\rm B}$ is derived by writing the magnetic energy as

$$E'_{\rm B} = \frac{B^2 M}{2\mu_0\rho}\qquad(A12)$$

and solving the critical mass for $E'_{\rm B} + E_{\rm G} = \frac{B^2 M}{2\mu_0\rho} - \frac{3}{5}\frac{GM^2}{R} < 0$. However, we point out that since M, ρ, and R are not independent ($M = 4\pi R^3 \rho/3$), the magnetic virial mass should be written as a function of R or ρ, but not both R and ρ. Thus $M'_{\rm B}$ does not accurately estimate the magnetic virial mass. For a magnetically supercritical ($M > M_{\rm B}$) structure, $M'_{\rm B} = \frac{10\pi R^4 B^2}{9\mu_0 GM} < \frac{10\pi R^4 B^2}{9\mu_0 GM_{\rm B}} = M_{\rm B}$ would underestimate the magnetic virial mass, and vice versa. For comparison with $M_{\rm B}$, the magnetic critical mass of an isothermal disk (Nakano, & Nakamura 1978) has been derived to be

$$M_{B,disk} = \frac{\pi R^2 B}{\sqrt{\mu_0 \pi G}}.\qquad(A13)$$

Crutcher et al. (2004) introduced a parameter λ to state the mass-to-flux ratio in units of its critical value:

$$\lambda = \frac{(M/\Phi)_{observed}}{(M/\Phi)_{critical}} = \frac{M}{M_{B,disk}},\qquad(A14)$$

where $(M/\Phi)_{observed}$ is the observed mass-to-magnetic-flux ratio:

$$(\frac{M}{\Phi})_{observed} = \frac{\mu_{\rm H_2} m_{\rm H} N(H_2)}{B},\qquad(A15)$$

and $(M/\Phi)_{critical}$ is the critical mass-to-magnetic-flux ratio:

$$(\frac{M}{\Phi})_{critical} = \frac{1}{\sqrt{\mu_0 \pi G}}.\qquad(A16)$$

For magnetically subcritical structure with mass less than the magnetic critical mass, the magnetic field alone can prevent the structure from collapse.

   Taking into account both the magnetic energy and the kinetic energy, a structure is stable when $2E_{\rm k} + E_{\rm B} + E_{\rm G} < 0$. The critical virial mass is calculated to be

$$M_{\rm k+B} = \sqrt{M_{\rm B}^2 + (\frac{M_{\rm k}}{2})^2} + \frac{M_{\rm k}}{2}.\qquad(A17)$$

It should be noted that $M_{\rm k} + M_{\rm B}$ is systematically larger than $M_{\rm k+B}$ (Bertoldi, & McKee 1992) and the largest ratio between $M_{\rm k} + M_{\rm B}$ and $M_{\rm k+B}$ is 1.25 when $M_{\rm B} = 0.67M_{\rm k}$, Therefore some previous studies using $M_{\rm B} + M_{\rm k}$ to represent the total virial mass may have slightly overestimated the support from the magnetic field and gas motion. Following the definition of α_k, we can define a total virial parameter

$$\alpha_{k+B} = \frac{M_{\rm k+B}}{M}.\qquad(A18)$$